DOE/JPL 954376-78/4
DISTRIBUTION CATEGORY UC-63

LASER-ZONE GROWTH IN A RIBBON-TO-RIBBON (RTR) PROCESS SILICON SHEET GROWTH DEVELOPMENT FOR THE LARGE AREA SILICON SHEET TASK OF THE LOW-COST SOLAR ARRAY PROJECT

ANNUAL REPORT

MOTOROLA REPORT NO. 2256/11

1 OCTOBER 1977 - 30 SEPTEMBER 1978

JPL CONTRACT NO. 954376

BY

A. BAGHDADI, R.W. GURTLER, R. LEGGE, B. SOPORI, R.J. ELLIS

PREPARED BY

MOTOROLA, INC.

SEMICONDUCTOR GROUP
5005 E. MCDOWELL ROAD
PHOENIX, ARIZONA 85008

THE JPL LOW-COST SOLAR ARRAY PROJECT IS SPONSORED BY THE U.S. DEPARTMENT OF ENERGY AND FORMS PART OF THE SOLAR PHOTOVOLTAIC CONVERSION PROGRAM TO INITIATE A MAJOR EFFORT TOWARD THE DEVELOPMENT OF LOW-COST SOLAR ARRAYS. THIS WORK WAS PERFORMED FOR THE JET PROPULSION LABORATORY, CALIFORNIA INSTITUTE OF TECHNOLOGY BY AGREEMENT BETWEEN NASA AND DOE.

MOTOROLA PROJECT NO. 2319 - 2325

(NASA-CR-158045) LASER-ZONE GROWTH IN A RIBBON-TO-RIBBON (RTR) PROCESS. SILICON SHEET GROWTH DEVELOPMENT FOR THE LARGE AREA SHEET TASK OF THE LOW-COST SOLAR ARRAY PROJECT Annual Report (Motorola, Inc.) N79-14547 Unclas G3/44 41948

THIS REPORT WAS PREPARED AS AN ACCOUNT OF WORK SPONSORED BY THE UNITED STATES GOVERNMENT. NEITHER THE UNITED STATES NOR THE UNITED STATES DEPARTMENT OF ENERGY, NOR ANY OF THEIR EMPLOYEES, MAKES ANY WARRANTY, EXPRESS OR IMPLIED, OR ASSUMES ANY LEGAL LIABILITY OR RESPONSIBILITY FOR THE ACCURACY, COMPLETENESS OR USEFULNESS OF ANY INFORMATION, APPARATUS, PRODUCT OR PROCESS DISCLOSED, OR REPRESENTS THAT ITS USE WOULD NOT INFRINGE PRIVATELY OWNED RIGHTS.

SUMMARY

This report includes a new calculation of the effects of thermal stresses during growth on silicon ribbon quality. Thermal stress distributions are computed for ribbon growth under a variety of temperature profiles. It is shown that the width dependence is not as large as had previously been assumed. Under practical growth conditions, the stresses are actually often below the yield point. It is also shown that, for the thermal profiles presently in use, buckling is probable for widths greater than 4 - 6 cm. Two "ideal" temperature profiles are described which could result in ribbons grown without either high dislocation generation or buckling.

We have now achieved a growth rate of 55 cm^2/min with a single ribbon. We have also demonstrated the growth of RTR ribbon with a fairly uniform parallel dendritic structure. The microstructure of this ribbon concentrates the most damaging defects into small areas between dendrites. This microstructure could result in an improved overall efficiency for cells fabricated on RTR ribbon.

We have obtained encouraging results with two approaches for reducing the Mo impurity level in polycrystalline feedstock. Neutron Activation Analysis has shown that the Mo level can be reduced to below the level of detection by etching the polycrystalline ribbon surface. Coating the Mo substrate with Si_3N_4 does not affect thermal shear separation of the polyribbon (Si_3N_4 is a well-known diffusion barrier); this process shows promise of improving cell efficiencies and also increasing the useful life of the molybdenum substrate.

A number of solar cells have been fabricated on RTR silicon grown from CVD feedstock. The highest efficiency (η ~ 6%) was obtained on a sample grown from a polyribbon deposited on a Si_3N_4 coated Mo substrate. This

result is disappointing. It may be due to incomplete coverage of the Mo substrate. We are now working with more uniform Si_3N_4 films of increased thickness.

TABLE OF CONTENTS

SECTION	TITLE	PAGE
1.0	Thermal Stress Analysis	1
1.1	The Model	3
1.2	Theoretical	7
1.3	Numerical Solution	9
1.4	Stress Distribution	10
1.4.1	Pure Parabolic	12
1.4.2	Limited-Extent Parabolic	14
1.4.3	Free-End Promimity Effects	17
1.4.4	Realistic Temperature Profiles	17
1.5	Thermal Profile Design	24
1.5.1	Profiles for Wide Ribbon Growth	29
1.6	Buckling of RTR Ribbons	30
1.6.1	Buckling Mechanisms	33
1.6.2	Discussion	37
1.7	Conclusion	38
2.0	Crystal Growth	39
2.1	Controlled Dendritic Growth	39
3.0	Silicon Tape Casting	51
4.0	Impurity Control in RTR Silicon	53
6.0	Solar Cells - Feedstock Grown on Bare Mo Substrate	62
6.1	Solar Cells - Feedstock Grown on Si_3N_4 - Coated Substrate	67
7.0	Problems	71

SECTION	TITLE	PAGE
8.0	Plans	72
8.1	Polycrystalline Feedstock	72
8.2	RTR Growth	72
8.3	Solar Cell Processing	72
9.0	New Technology	74

LIST OF FIGURES

FIGURE NUMBER	TITLE	PAGE
1	Photograph of 7.5 cm wide RTR ribbon grown at 5 cm/min. Significant buckling is evident.	2
2	Sample geometry for theoretical analysis.	8
3	Mesh definition for numerical analysis. K_x and K_y are integers which increase the density of the mesh for the distance Sx to give improved accuracy and where large variations in temperature occur.	11
4	Normalized stress distributions for a 2 cm wide sample with the temperature profile T5 of Figure 7.	13
5	Linear-parabolic-linear temperature profiles. The parabolic-linear transitions are noted for each profile.	15
6	Stress distributions for a 2 cm wide sample with the various temperature profiles of Figure 5.	16
7	Linear-parabolic-linear temperature profiles imposed at various locations with respect to a free end. The resulting stress distributions are shown in Figure 8.	18
8	Stress distributions resulting from a linear-parabolic-linear temperature profile imposed at various distances from the free end (melt) of a 2 cm wide ribbon.	19
9	Width dependence of stresses resulting from a parabolic-linear temperature profile (T5 of Figure 7) imposed near the free end (melt) of a ribbon.	20
10	A "real" ribbon growth temperature profile is a composite of a laser-only (theoretical) and furnace-only (measured) profile. Also shown is a linearized version of the composite profile which simplified the numerical analysis.	21
11	Stress distributions in a 6 cm wide ribbon under the influence of (a) a laser-only profile, (b) a furnace-only profile and (c) a composite profile which might be typical of actual growth conditions.	23

FIGURE NUMBER	TITLE	PAGE
12	Width dependence of stresses in a ribbon with the composite temperature profile of Figure 10.	25
13	"Ideal" profile exhibiting a perfectly linear distribution from the melt down to a temperature of 600°C, then parabolically approaching an ambient temperature of 100°C.	27
14	Stress distributions arising from the "ideal" profile of Figure 13. For wide samples, very large stresses result.	28
15	Profile improvements which can lead to improved, wide ribbon growth conditions. T2 represents conditions expected when the melt is moved closer to the postheater. T3 represents an ideal profile which achieves high growth velocity and low stresses (see Figure 16).	31
16	Stress distributions for the profiles of Figure 15.	32
17	Thin plate acted on by uniform compressive stresses in the plane of the plate. For stresses exceeding a critical stress, σ_{cr}, the plate becomes unstable and buckling can occur.	34
18	CVD ribbon: The black dots are the nodules containing the growth spikes referred to in the text.	40
19a	RTR sample grown from feedstock containing growth spikes.	41
19b	RTR sample grown from feedstock which did not contain growth spikes.	41
20	Temperature profile across ribbon width.	43
21	Dendrite nucleation.	44
22	Surface topography - controlled dendrite growth.	45
23	Surface topography - random dendrite growth.	46
24	Dendrite microstructure.	48
25	Grain boundary.	49
26	End view of planar defect.	50
27	Mo concentration - depth profile.	55

FIGURE NUMBER	TITLE	PAGE
28	Microcrack in Si_3N_4 film (400X magnification).	56
29	Diffusion length measurement by DWM - Sample 784-1.	59
30	Semilogarithmic current-voltage characteristics--regrown single crystal and CVD cells.	64
31a	Ribbon fracture -- parallel to growth.	65
31b	Ribbon fracture -- normal to growth.	65

1.0 THERMAL STRESS ANALYSIS

In the evolution of current ribbon crystal growth technologies, the role of thermally induced stresses has been one of a major antagonist. In early stages of development, fracture due to residual stresses arising from thermal non-linearities near the growth interface, led to severe limitations for growth velocity and ribbon width. With the addition of well designed postheaters (and in the case of RTR growth, preheaters) residual stresses have been all but eliminated [1]. This is not to say, however, that thermal stresses near the growth interface have been eliminated; all that has been achieved is relief of built-in stresses as the ribbon passes through the postheater. Substantial thermal stresses remain throughout the growth region and their presence is manifested in the generation of dislocations and ribbon buckling. Dislocations can lead to reductions in minority carrier lifetime [2] which can result in low photovoltaic efficiencies. Buckling (see Figure 1) leads to difficulties in automated processing of ribbons, e.g., transport mechanisms, photolithography, etc.

Because of these adverse effects, it is of importance to have a better understanding of the nature of thermal stresses in a ribbon growth environment. One study of this type has already been reported by Surek [3]. In that paper, an analytic treatment was presented; it was not actually appropriate, as was pointed out in the paper. Nevertheless, some general trends indicated from that analysis implied that stress levels would increase very rapidly with sample width. To remedy the deficiencies of the analytical treatment, a numerical solution which confirmed the deficiencies of the analytic treatment was also described. However, no data were presented from the numerical approach. A more

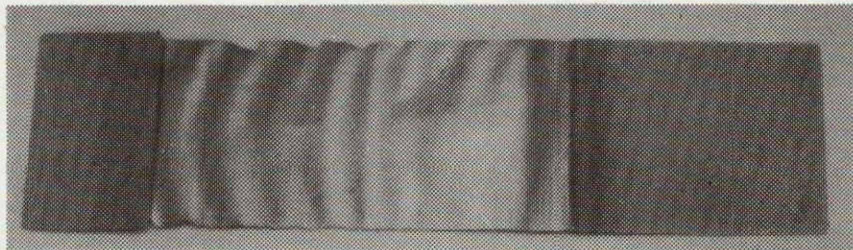

10 cm

E8743

FIGURE 1: Photograph of 7.5 cm wide RTR ribbon grown at 5 cm/min. Significant buckling is evident.

ORIGINAL PAGE IS
OF POOR QUALITY

effectiveness of stress relief, especially near the melt zone, towards reduction of stresses. Stress relief is a dynamic process and in the immediate vicinity of the melt, stresses are rapidly changing. As will be shown, for a wide sample (e.g. 6 cm wide) at growth velocities of 8 cm/min, elastic strain rates of $10^{-5} sec^{-1}$ to over $10^{-4} sec^{-1}$ can be deduced with stresses in excess of $6x10^8$ dynes/cm^2. If effective stress relaxation is to occur, viscoelastic strain rates at these stress levels should be orders of magnitude higher. Myshlyaev [4] and Graham [5] have studied single and polycrystalline silicon for temperatures in the range of 900°C to greater than 1300°C. Considering the nature of RTR ribbon, possibly one should expect that material properties characteristic of polycrystalline silicon should be most appropriate although ribbon grain sizes are considerably larger. Graham finds that at 1380°C and at strain rates of $8x10^{-4} sec^{-1}$, a stress level of $2.75x10^8$ dynes/cm^2 is required. Grahams' data, while on polycrystalline material, are not inconsistent with that of Myshlyaev on single crystal samples. Myshlyaev arrives at the following expression for flow stresses in single crystal silicon for the studied temperature range (900°C - 1300°C):

$$\dot{\varepsilon} = \dot{\varepsilon}_o \exp \left[\frac{-(u_o - V\sigma)}{kT}\right] \quad (1)$$

$\dot{\varepsilon}_o = 10^{11} sec^{-1}$

$U_o = 5.6$ eV

$V = 2.7x10^{-21} cm^3$

σ = Shear stress in dynes/cm^2

U_o is the activation energy required for dislocation movement while $V\sigma$ can be thought of as the barrier reduction due to the presence of the stress field σ. Inverting this we find for the shear stress required to achieve a given strain rate $\dot{\varepsilon}$ is -

$$\sigma_Y = \frac{kT}{V} \ln \frac{\dot{\varepsilon}}{\dot{\varepsilon}_o} + \frac{U_o}{V} \qquad (2)$$

Defining a yield stress as that stress required to achieve a strain rate of 10^{-5} sec^{-1}, we arrive at Table I. Also shown are normalized yield stresses, $\hat{\sigma}_y = \sigma_y/\alpha E$, where α is the thermal expansion coefficient and E is Young's modulus. We have assumed $\alpha = 4x10^{6}$, $E = 1.17x10^{12}$ dynes/cm^2 or $\alpha E = 4.68x10^6$ dynes/cm^2. Most stresses in this paper will be normalized.

These data are reasonably consistent with that of Sylwestrowicz [6] who also has studied single crystal silicon properties for temperatures of 600°C - 1345°C. While the highest stress for the RTR growth example cited was $4.12x10^8$ dynes/cm^2, most regions of stress are considerably lower and consequently are below the yield stress levels of Table I.

Patel et. al. [7] have also studied the flow stress behavior of silicon up to temperatures of 1000°C, although their primary emphasis was towards germanium. Their results appear to be in considerable disagreement with the other investigators. Their findings at 1000°C are about one order of magnitude lower than those indicated in Table I. Furthermore, they present a curve for flow stress vs. temperature which would, if extrapolated, fall far below that of Table I. The reason for this disagreement (although Patel et. al. claimed in their paper to be consistent with the measurements by Sylwestrowicz) is not clear, but the fact that measurements were limited to 1000°C leads one to accept the measurements by Graham, Sylwestrowicz and Myshlyaev as more appropriate.

TABLE I

SILICON YIELD STRESSES

($\ddot{\varepsilon} = 10^{-5}$ sec, $\alpha E \sim 4.68 \times 10^{6}$)

T	900°C	1000°C	1100°C	1200°C	1300°C	1400°C
σ_Y	11.12×10^{8}	9.23×10^{8}	7.35×10^{8}	5.47×19^{8}	3.58×10^{8}	1.7×10^{8}
$\hat{\theta}_Y$	267	197	157	116	76	36

These data then indicate that in a dynamic situation such as RTR growth, sizeable in situ stresses may be sustained even at temperatures near that of the melt, and that a yield stress concept may be usefully employed. Correspondingly, the stresses implied by the elastic analysis of real thermal profiles and wide ribbons will be shown to be commensurate with these yield stresses, thus indicating the possibility of wide ribbon growth without excessive plastic strain if further improvements in thermal profile are made.

Ribbon buckling also attests to the presence of in situ stresses. Using classical results from the theory of elastic instability, it will be shown that buckling can be expected for wide sample growth unless improved thermal profiles are achieved.

1.2 Theoretical

Figure 2 indicates the geometry considered for the study. In cases of practical interest, the sample width (2C) and length are much greater than the sample thickness. In this case it can be assumed that thickness components of stress vanish in comparison to in-plane components, i.e. $\sigma_{zz} = \sigma_{xz} = \sigma_{yz} = 0$. This is a condition of plane stress and the stresses may be found from solutions of the biharmonic equation [8]

$$\nabla^4 \phi = -\alpha E \nabla^2 T$$

or

$$\partial_x^4 \phi + 2\partial_y^2 \phi + \partial_y^4 \phi = -\alpha E \left(\partial_x^2 T + \partial_y^2 T\right) \qquad (3)$$

where

$$\sigma_{xx} = \partial_{yy}^2 \phi$$

$$\sigma_{yy} = \partial_{xx}^2 \phi$$

$$\sigma_{xy} = -\partial_{xy}^2 \phi$$

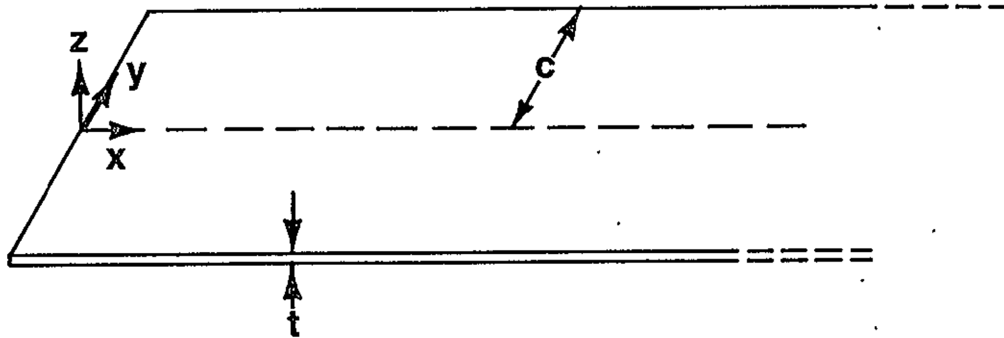

FIGURE 2: Sample geometry for theoretical analysis.

and α,E are the expansion coefficient and modulus of elasticity respectively. Boundary conditions on ϕ are required for a unique solution. At the melt (x = 0) and at y = ±C exist free boundaries, and on these boundaries it can be shown that the boundary conditions are

$$\phi = \partial_n \phi = 0 \qquad (4)$$

where ∂_n denotes the derivative normal to the surface. In this study, temperature variations are assumed to be entirely x dependent (i.e. $\partial_y T = \partial^2_y T=0$); consequently symmetry may be invoked about y = 0. Boundary conditions along y = 0 therefore are:

$$\partial_y \phi \Big|_{y=0} = 0$$

$$\phi(x,y)=\phi(x,-y) \qquad (5)$$

Finally, since a numerical solution is to be obtained, a boundary condition must be imposed at x=L where L is the length of the ribbon segment. In this case it is assumed that the temperature distribution at x=L is slowly varying with at most a parabolic dependence. "Slowly" is a situation specific term and in practice means that the curvature is hardly changing over distances comparable to the ribbon width. Under these conditions ϕ can be shown by analytic means [9] to be

$$\phi(L,y) = -\frac{\alpha E}{24} (y^2-C^2)^2 \, d^2_x T \qquad (6)$$

1.3 Numerical Solution

Numerical solutions were obtained by the technique of finite differences using the Gauss-Seidel iterative relaxation technique. Because of the occurrence of thermal profiles exhibiting very large

gradients and curvatures near $x=0$, the rectangular variable mesh system of Figure 3 was utilized. This allowed a much finer resolution near the melt where detail was necessary. For a rectangular mesh, the symbolic representation [10] for the finite difference weighting of neighboring points for equation (3) is

$$\left\{\begin{matrix} 0 & 0 & \frac{1}{h_y^4} & 0 & 0 \\ 0 & \frac{2}{h_x^2 h_y^2} & -\left(\frac{4}{h_y^4} + \frac{4}{h_x^2 h_y^2}\right) & \frac{2}{h_x^2 h_y^2} & 0 \\ \frac{1}{h_x^4} & -\left(\frac{4}{h_x^4} + \frac{4}{h_x^2 h_y^2}\right) & \left(\frac{6}{h_x^4} + \frac{8}{h_x^2 h_y^2} + \frac{6}{h_y^4}\right) & -\left(\frac{4}{h_x^4} + \frac{4}{h_x^2 h_y^2}\right) & \frac{1}{h_x^4} \\ 0 & \frac{2}{h_x^2 h_y^2} & -\left(\frac{4}{h_y^4} + \frac{4}{h_x^2 h_y^2}\right) & \frac{2}{h_x^2 h_y^2} & 0 \\ 0 & 0 & \frac{1}{h_y^4} & 0 & 0 \end{matrix}\right\} \phi = -\alpha E \partial_x^2 T \qquad (7)$$

where h_x and h_y are the node separations in the x and y directions. During computation, an overrelaxation constant of 1.75 was utilized and iterations were continued usually until the stress potential at a key point changed by less than one part in 10^6 per iteration. In some cases, notably very wide samples, somewhat less accuracy was accepted. Depending on the width of the sample, the coarse node separation was typically 1 - 2 mm while the fine resolution node separation was as small as .25 mm.

1.4 Stress Distributions

Because there is no simple way to present complete stress distributions in detail (three components σ_{xx}, σ_{yy}, σ_{xy} each a function of

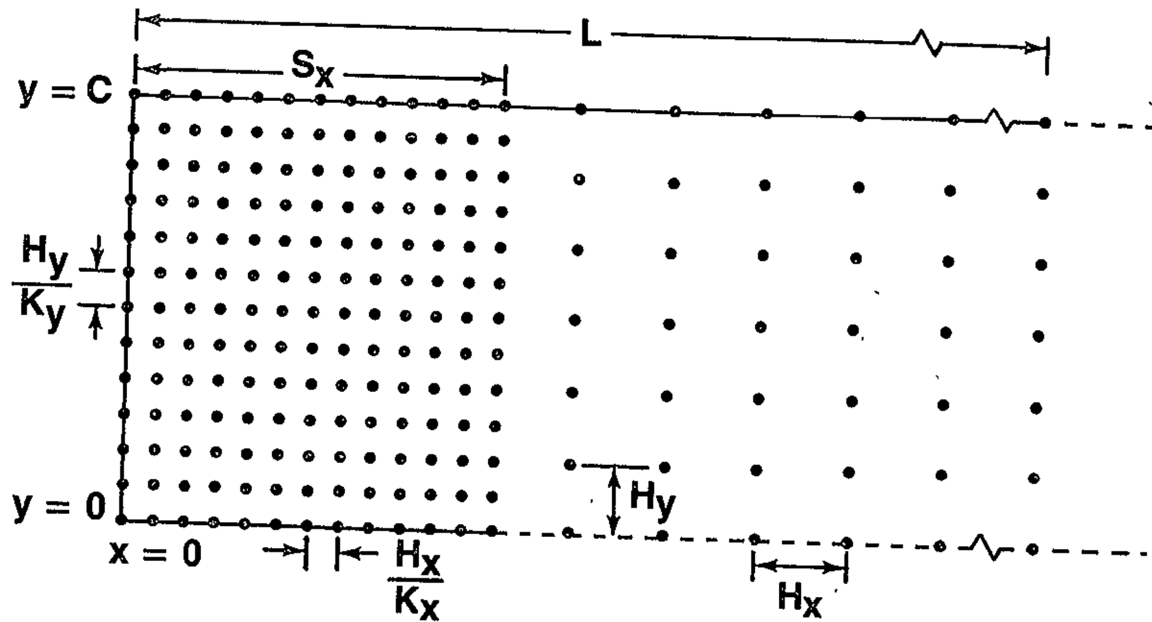

FIGURE 3: Mesh definition for numerical analysis. K_x and K_y are integers which increase the density of the mesh for the distance Sx to give improved accuracy and where large variations in temperature occur.

x and y), only selected distributions will be shown. First will be presented in some detail a very simple example which illustrates roughly the general behavior of all distributions. Then subsequent distributions will be considerably abbreviated.

1.4.1 Pure Parabolic

As a first example, which illustrates many important aspects of the nature of ribbon stress distributions, and the effects of a free boundary (melt region), a pure parabolic temperature distribution is assumed, i.e.,

$$d_x^2 T = \text{constant} = 400^\circ C/cm^2 \qquad (8)$$

(See for example curve #T5 of Figure 7).

While such a temperature distribution is nonphysical, (rapidly exceeding the melting point of silicon), it is simple to treat far away from the free end (x=0) and in fact is given by equation (6). From equation (3) we find that for x>>C

$$\sigma_{xx} = -\frac{1}{6}(3y^2 - C)\, d_x^2 T \qquad (9)$$

$$\sigma_{yy} = \sigma_{xy} = 0$$

For C = 1 cm, $d_x^2 T = 400^\circ C/cm^2$, we have

$$\sigma_{xx} = -66.7\,(3y^2 - 1) \qquad (10)$$

Thus, far from the end, only longitudinal stresses exist which vary quadratically with y. Figures 4a - 4f illustrate the calculated stress distributions. Note the pronounced effect of the free edge. While

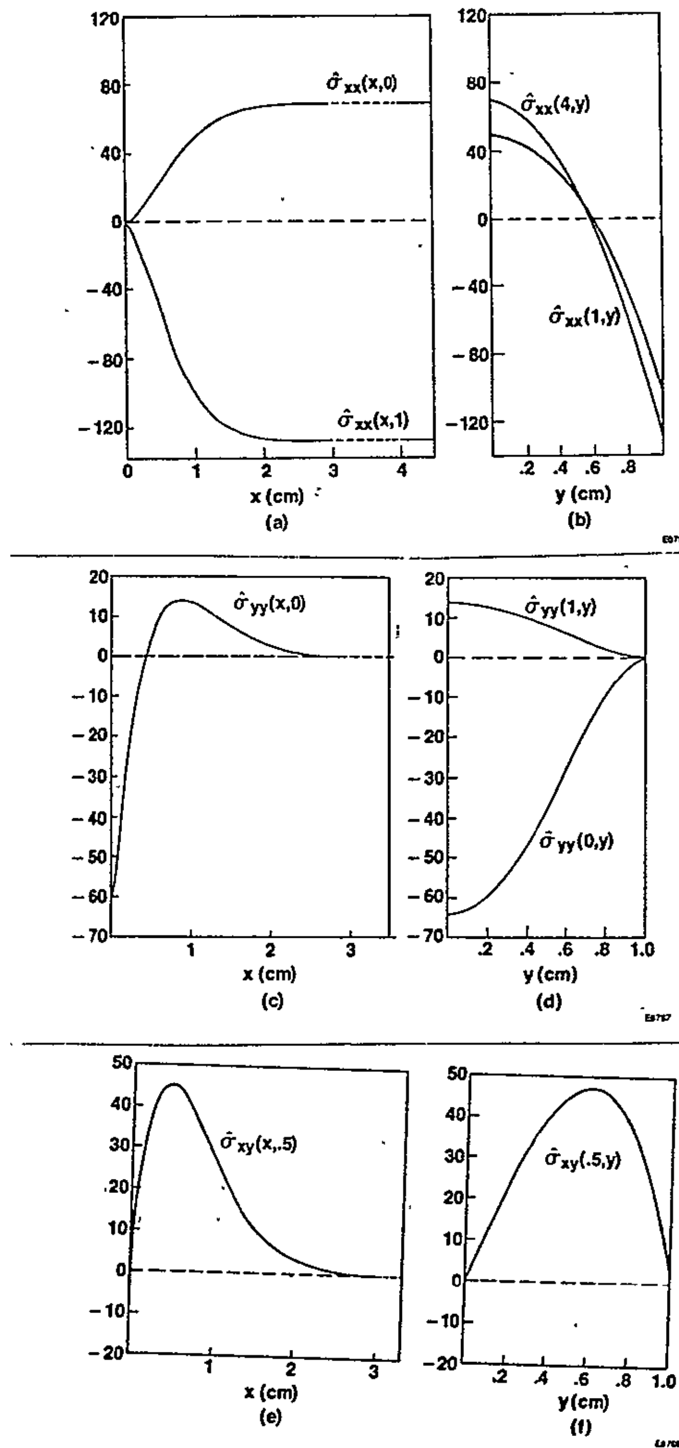

ORIGINAL PAGE IS
OF POOR QUALITY

FIGURE 4: Normalized stress* distributions for a 2 cm wide sample with the temperature profile T5 of Figure 7.

* The stresses are all normalized to the dimensionless parameter $\hat{\sigma} = \sigma/\alpha E$, where α is the thermal expansion coefficient and E is Young's modulus.

σ_{xx} is large and $\sigma_{yy} = 0$ for x large, the reverse is true at x = 0; there, $\sigma_{xx} = 0$ and σ_{yy} is large. In the region $0 < x \leq 2$, shear stresses (σ_{xy}) temporarily become large, and σ_{yy} alternates in sign and damps to zero. Note the good agreement of the numerical solution with the analytical solution far from the edge.

This complex behavior has arisen, not because of a complex temperature distribution, but simply because of the presence of a free edge in a simple non-linear temperature distribution. The dominance of lateral and shear stresses in the vicinity of the melt is characteristic of ribbon stresses.

1.4.2 Limited-Extent Parabolic

Another simple example illustrates that a non-linearity acting over a short distance will lead to considerably lower stresses as compared to a non-linearity which acts over a length sufficient to produce fully developed stresses. Figure 5 illustrates several linear-parabolic-linear temperature profiles, each with an equal curvature of $400^{\circ}C/cm^2$ in the central parabolic region, but with the parabolic profile extending over various "interaction" lengths. The center of the curved portion is placed 3 cm from the end of a 2 cm wide sample.

Figures 6a and 6b show computed stresses for the various cases. Also included is the pure parabolic stress distribution for comparison. Note that only for an interaction length of approximately the width of the ribbon do peak stresses approach that of the pure parabolic distribution while shorter interaction lengths give progressively lower stresses.

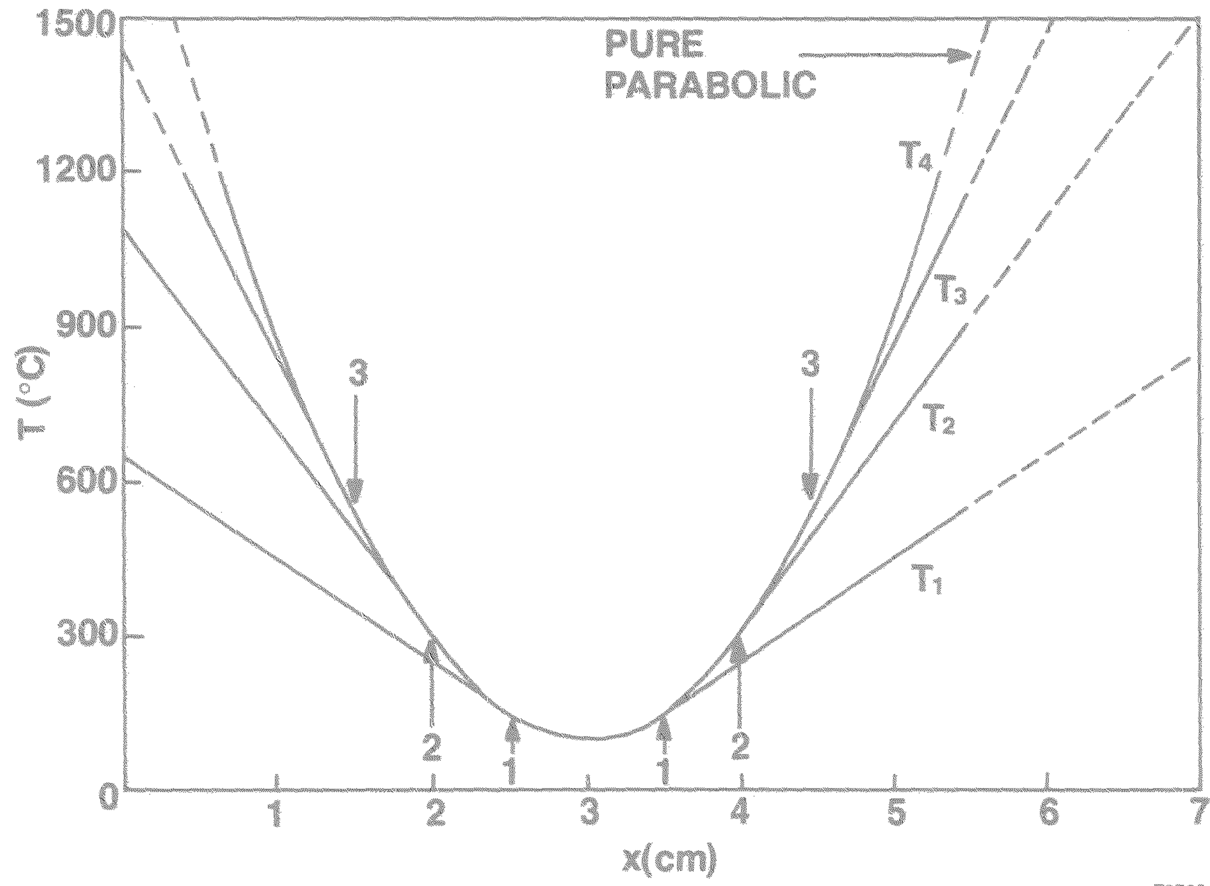

FIGURE 5: Linear-parabolic-linear temperature profiles. The parabolic-linear transitions are noted for each profile.

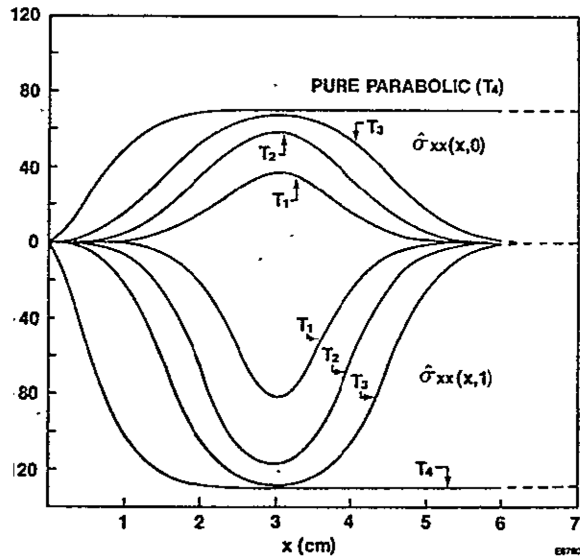

(A)

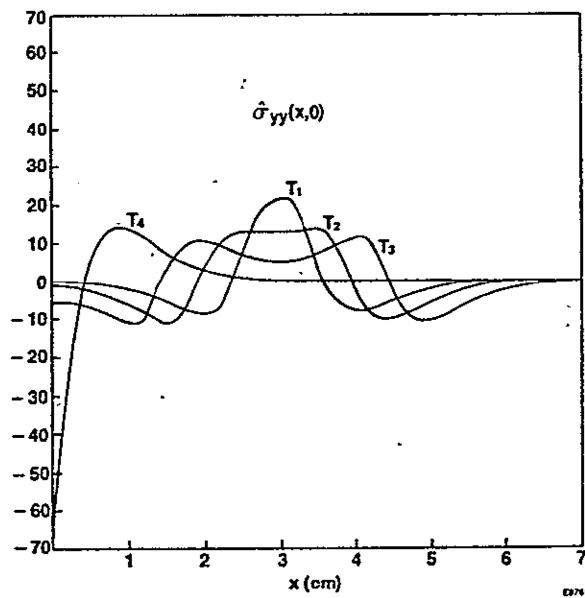

(B)

FIGURE 6: Stress* distributions for a 2 cm wide sample with the various temperature profiles of Figure 5.

* The stresses are all normalized to the dimensionless parameter $\hat{\sigma} = \sigma/\alpha E$, where α is the thermal expansion coefficient and E is Young's modulus.

1.4.3 Free-End Proximity Effects

If a given thermal non-linearity is brought close to the free end, the nature of the stresses, and their magnitude, change dramatically. Figure 7 illustrates various linear-parabolic-linear temperature profiles of equivalent shape (interation length = .5 cm = C/2, $d_x^2T = 800^oC/cm^2$) but acting at various distances from the free end. Figures 8a and 8b illustrate the resulting stresses. Note the damping of the longitudinal stresses but progressively increasing lateral stresses as the center of interaction approaches the end.

As a final example illustrating general trends, we consider the effects of sample width for the parabolic-linear temperature profile of Figure 7 when the parabolic region is closest to the end (T5). Figures 9a and 9b indicate the stress distribution for sample widths (2C) of 1 - 8 cm. While equation (9) would indicate that fully developed (longitudinal) stresses would vary as C^2, a much reduced variation is observed in Figure 9. This is a result of a non-linearity both being of limited extent and occurring quite near to the free end. Lateral stresses, however, do increase rapidly at first, but for the widest sample, a saturation is observed.

1.4.4 Realistic Temperature Profiles

The above considerations have indicated some important trends for ribbon shaped samples under the influence of various parabolic or piecewise-parabolic temperature profiles. Real temperature profiles are more complex. For example, Figure 10 depicts the various contributions to a real temperature profile. Shown are the calculated [11] temperature profile for a .15 mm thick ribbon which is laser melted, an actual

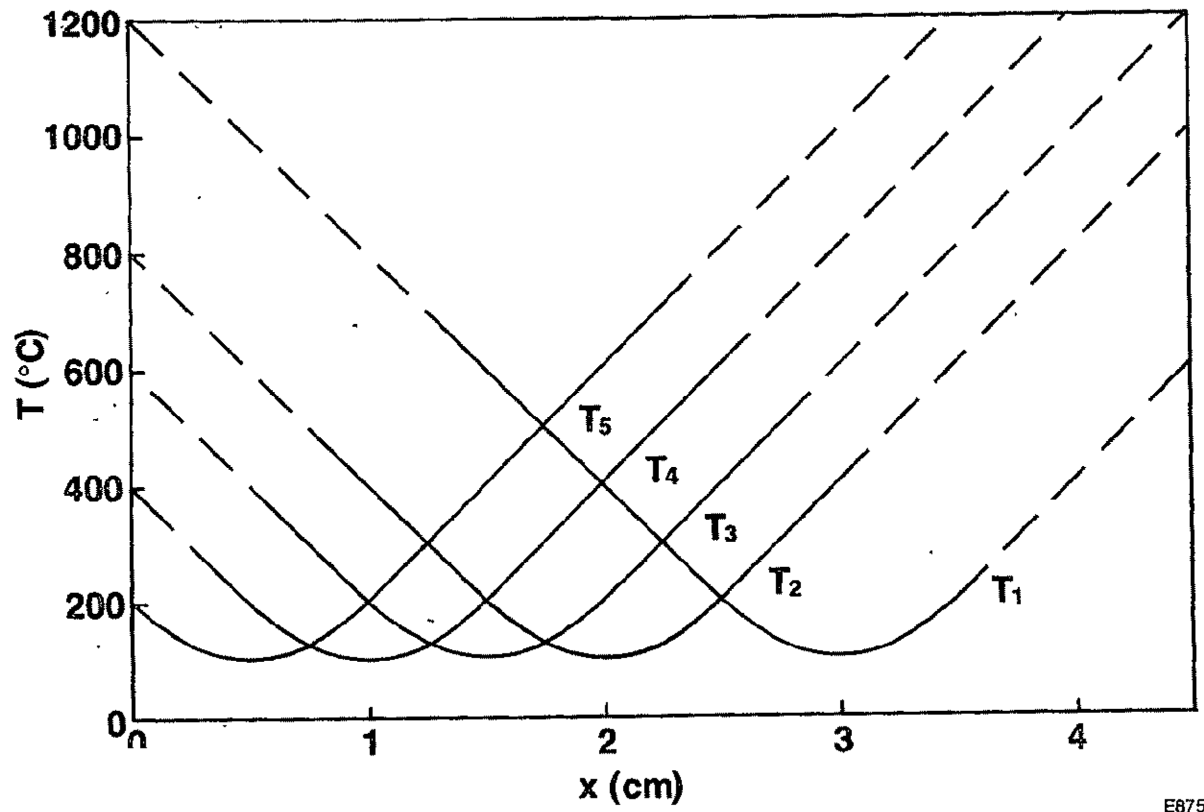

FIGURE 7: Linear-parabolic-linear temperature profiles imposed at various locations with respect to a free end. The resulting stress distributions are shown in Figure 8.

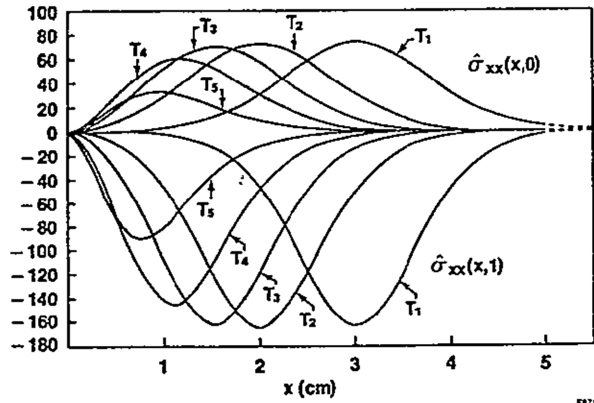

(A)

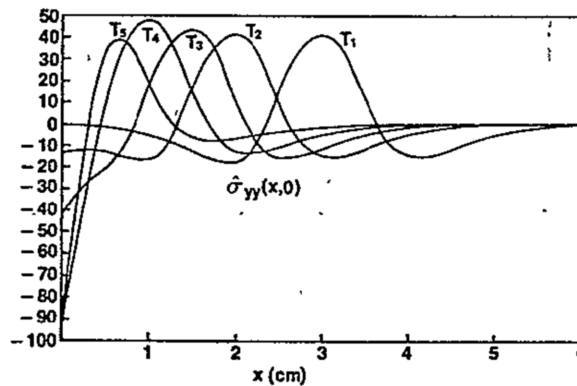

(B)

FIGURE 8: Stress* distributions resulting from a linear-parabolic-linear temperature profile imposed at various distances from the free end (melt) of a 2 cm wide ribbon.

* The stresses are all normalized to the dimensionless parameter $\hat{\sigma} = \sigma/\alpha E$, where α is the thermal expansion coefficient and E is Young's modulus.

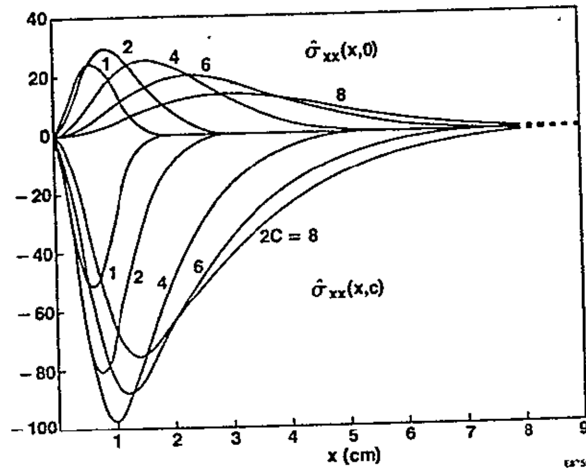

(A)

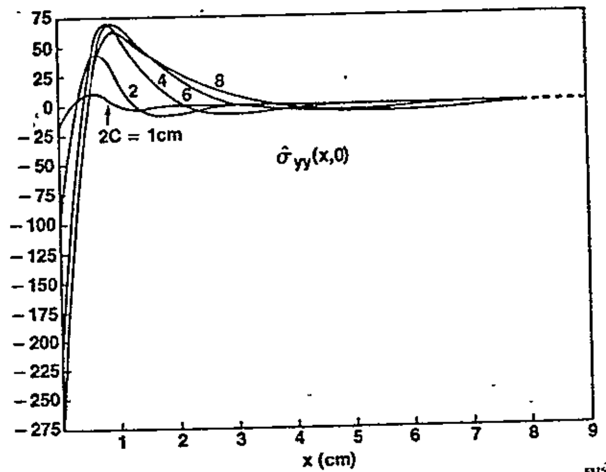

(B)

FIGURE 9: Width dependence of stresses*resulting from a parabolic-linear temperature profile (T5 of Figure 7) imposed near the free end (melt) of a ribbon.

* The stresses are all normalized to the dimensionless parameter $\hat{\sigma} = \sigma/\alpha E$, where α is the thermal expansion coefficient and E is Young's modulus.

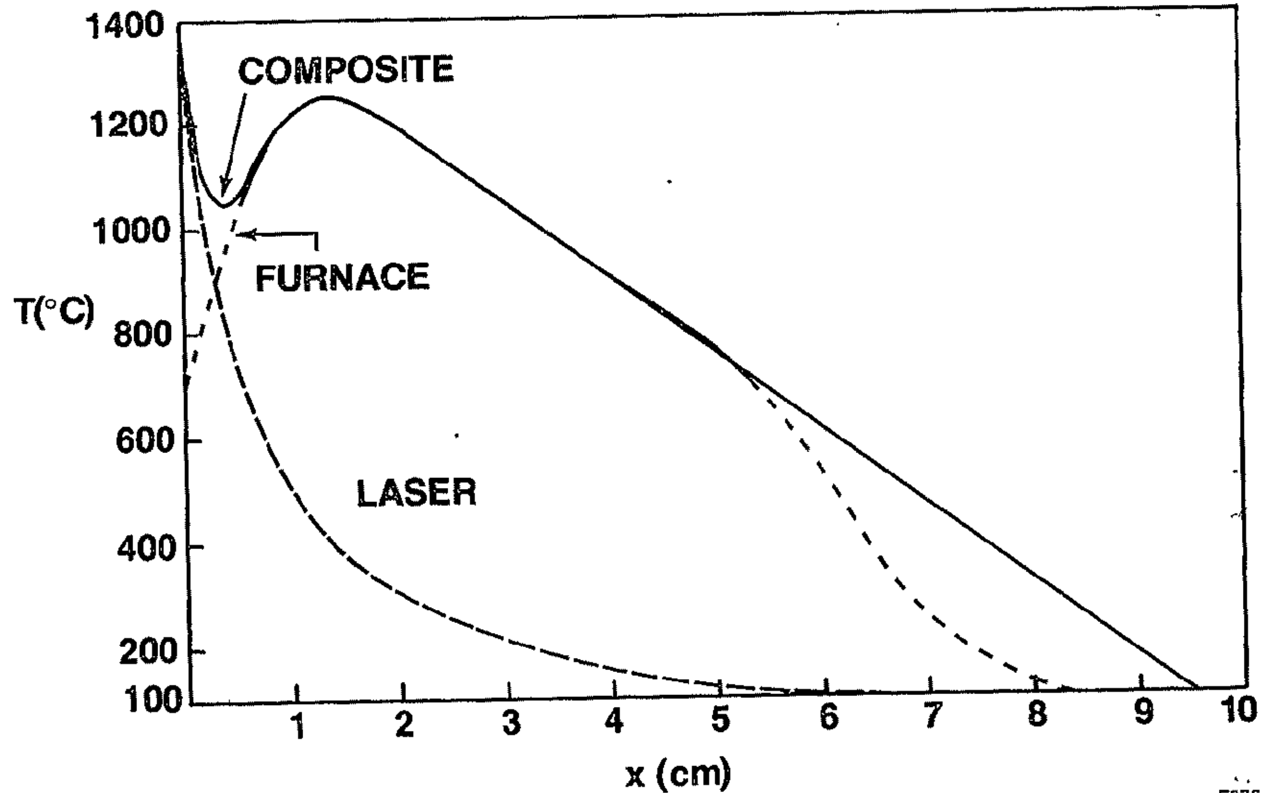

FIGURE 10: A "real" ribbon growth temperature profile is a composite of a laser-only (theoretical) and furnace-only (measured) profile. Also shown is a linearized version of the composite profile which simplified the numerical analysis.

(smoothed) furnace profile as measured by thermocouple profiling, and an intuitive, composite temperature profile which results when the laser and furnace are simultaneously used. Also shown, for simplification of analysis, are linearized versions of the furnace and composite profiles.

It is interesting to calculate separately the stresses which would be caused by the laser-only profile, the linearized furnace-only profile and then the linearized composite profile.

The laser-only profile is typical of actual growth conditions during early RTR development. This profile is very steep and has very high, and variable, curvature near the melt. This particular profile has a curvature of $18,000^{\circ}C/cm^2$ at x=0, $1200^{\circ}C/cm^2$ at x=.5 cm and dropping to $325^{\circ}C/cm^2$ at X=1 cm. Consequently, it might be expected that very large stresses would be encountered. Figures 11a and 11b relate the computed stresses for each of the profiles for a sample width of 6 cm. We see that qualitatively and quantitatively, the resulting stress distributions are quite different. Furthermore, the composite profile which approximates actual growth conditions, results in a stress distribution with surprising aspects. The composite profile appears to be more complex than either the furnace-only or laser-only profiles, yet the resulting stresses are considerably reduced in magnitude and extent. Even the lateral and shear stresses are markedly reduced as compared to the component profile stresses.

The new effect being observed here is the interaction of positive and negative curvature regions which tend to produce cancelling stresses. (In fact, superposition could be used, as the equations are linear, but the composite profile is not simply the sum of the component temperature profiles.)

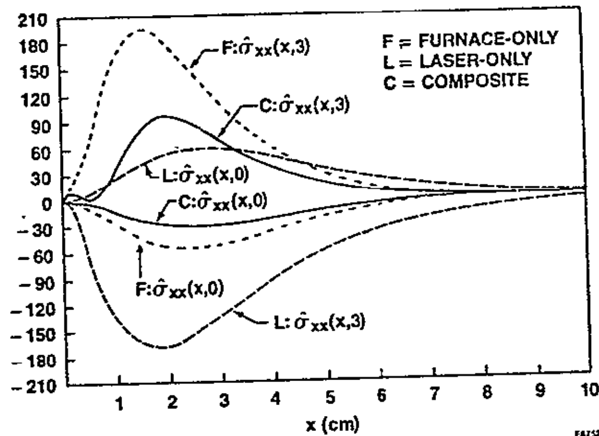

(A)

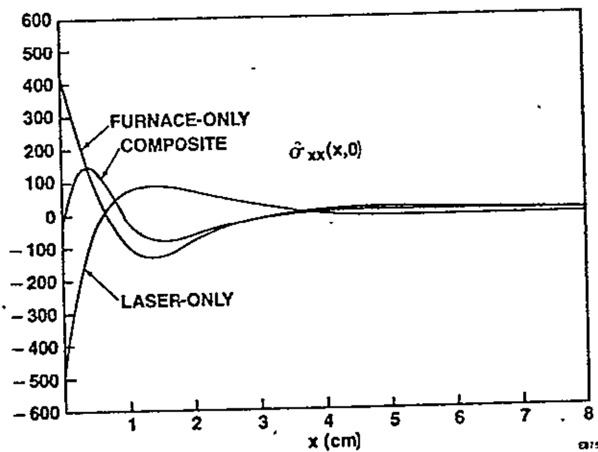

(B)

ORIGINAL PAGE IS
OF POOR QUALITY

FIGURE 11: Stress* distributions in a 6 cm wide ribbon under the influence of (a) a laser-only profile, (b) a furnace-only profile and (c) a composite profile which might be typical of actual growth conditions.

* The stresses are all normalized to the dimensionless parameter $\hat{\sigma} = \sigma/\alpha E$, where α is the thermal expansion coefficient and E is Young's modulus.

Figures 12a and 12b show the effects of width variation for the composite profile. These figures bring out another new aspect. The relatively simple symmetry between the central and edge longitudinal stresses no longer holds. As a function of width, the central stresses remain relatively simple while the edge stresses exhibit significant variations with width; the narrower samples following more closely the expected behavior for the particular thermal profiles.

Finally, we note that virtually all stresses indicated are below the yield stresses of Table 1 (comparison must be made on a point-by-point basis for stresses of Figure 12 and corresponding temperatures of Figure 10). The only exceptions are lateral stresses immediately adjacent to the melt. Of course, stress relief _will_ occur throughout the growth region but these calculations indicate that the plastic strain rate will usually be too low to totally relieve the stresses.

1.5 Thermal Profile Design

In considering further improvements in the thermal profile, we are assuming that insight gained from the study of an elastic model will be helpful because any stress reduction achieved on this basis, should lead to reduced dislocation generation, reduced buckling (see below) and generally improved crystal quality. From equation (3), and from the numerous examples cited previously, it would seem that the ideal profile would simply be a linear profile, i.e. $\partial_x^2 T=0$. (More generally, if $\nabla^2 T=0$ stresses would also vanish but considerations of this type lead us too far astray for the present discussion.) A strictly

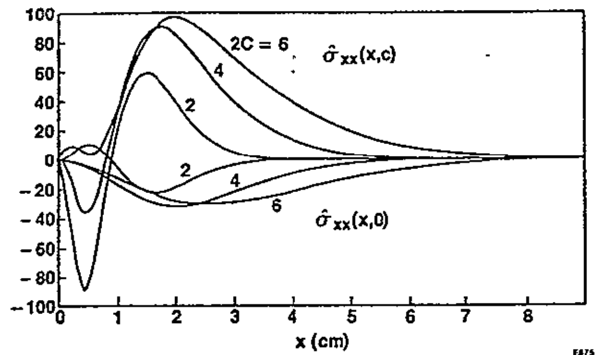

(A)

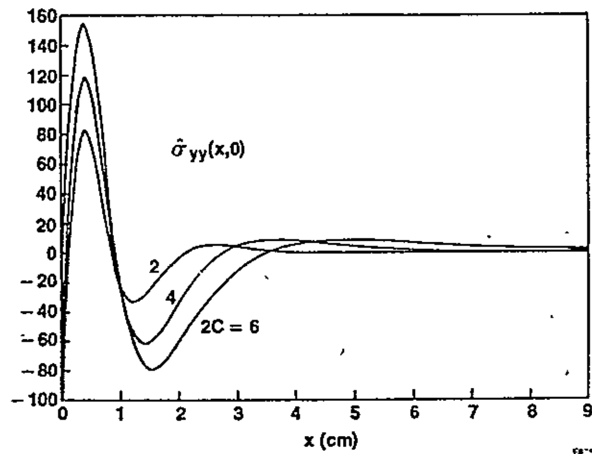

(B)

FIGURE 12: Width dependence of stresses* in a ribbon with the composite temperature profile of Figure 10.

* The stresses are all normalized to the dimensionless parameter $\hat{\sigma} = \sigma/\alpha E$, where α is the thermal expansion coefficient and E is Young's modulus.

linear profile is not possible, however, since at some point a minimum temperature will be reached which necessitates a region where $\partial_x^2 T \neq 0$. For example, in order to achieve high growth velocities, a steep temperature profile is required at the melt which ensures latent heat of fusion extraction from the melt. Otherwise, the melt width becomes large and growth will become unstable [11]. For a growth velocity v, thermal conductivity K, and a latent heat of fusion per unit volume H, then the thermal gradient at the melt must be of the order of

$$\partial_x T\Big|_{x=0} = -\frac{vH}{K} \tag{11}$$

If, for example, v = 2.5 cm/min = .0417 cm/sec, K = .23 w/cm/$^{\circ}$K, H = 4200 J/cm^3, then

$$\partial_x T\Big|_{x=0} \approx -750^{\circ}\mathrm{C/cm} \tag{12}$$

Consequently, even if a linear profile of this gradient were established, it could extend for a distance no longer than

$$L = \frac{T_M}{|\partial_x T|} \approx 2.25 \text{ cm} \tag{13}$$

since the temperature of the ribbon would then be absolute zero.

As an example of a realistic "ideal" profile, let us consider the profile of Figure 13. In this case we impose an initial gradient of 750°C/cm which is held constant down to a temperature of 600°C and is then allowed to parabolically approach an ambient of 100°C. Such a profile might actually be achieved in the RTR process if scanned and modulated laser or electron beams were used to force the desired profile. Figures 14a and 14b illustrate the resulting stresses for small ribbon widths. It is evident that for ribbon widths of current interest, e.g. >> 2 cm wide, no benefit is achieved by this profile and, in fact, stresses are worse than achieved with our present type of profile (Figures 12a, b).

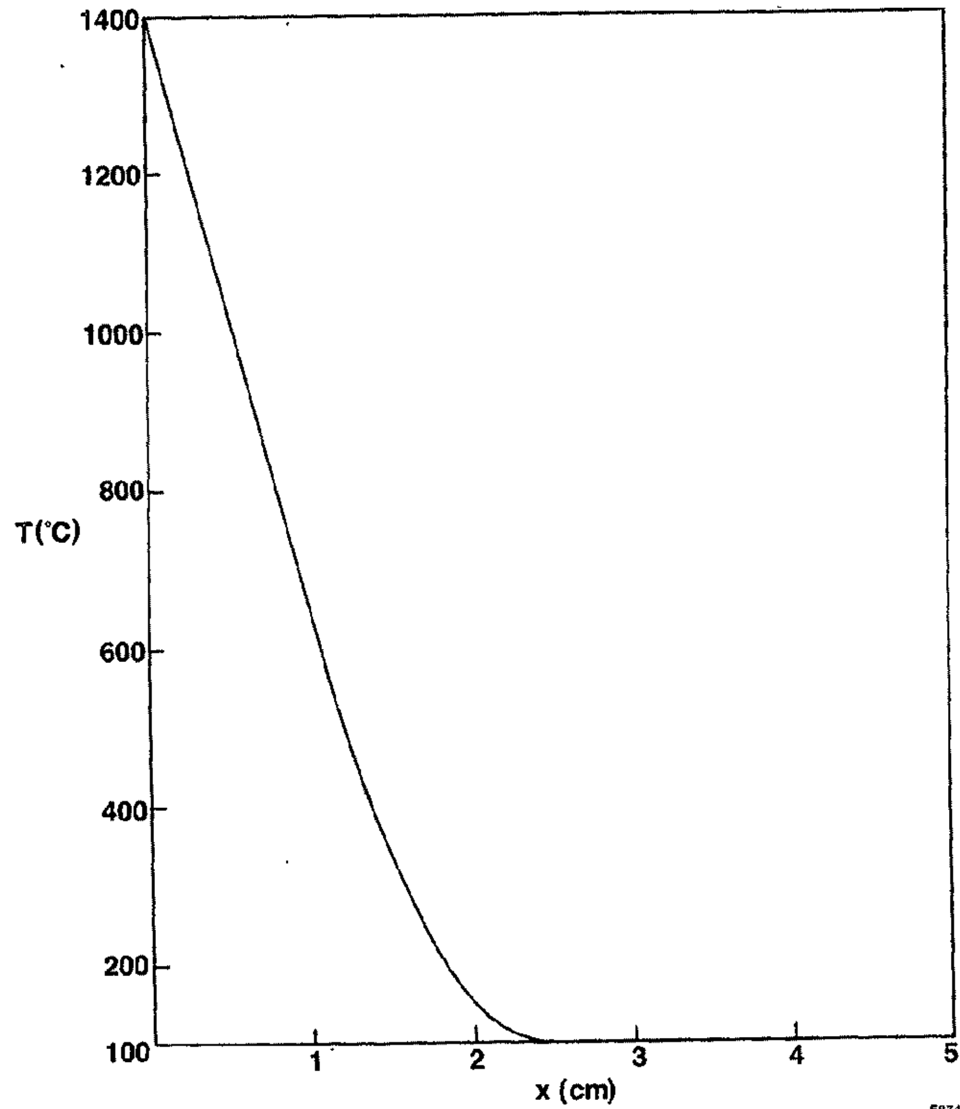

FIGURE 13: "Ideal" profile exhibiting a perfectly linear distribution from the melt down to a temperature of 600°C, then parabolically approaching an ambient temperature of 100°C.

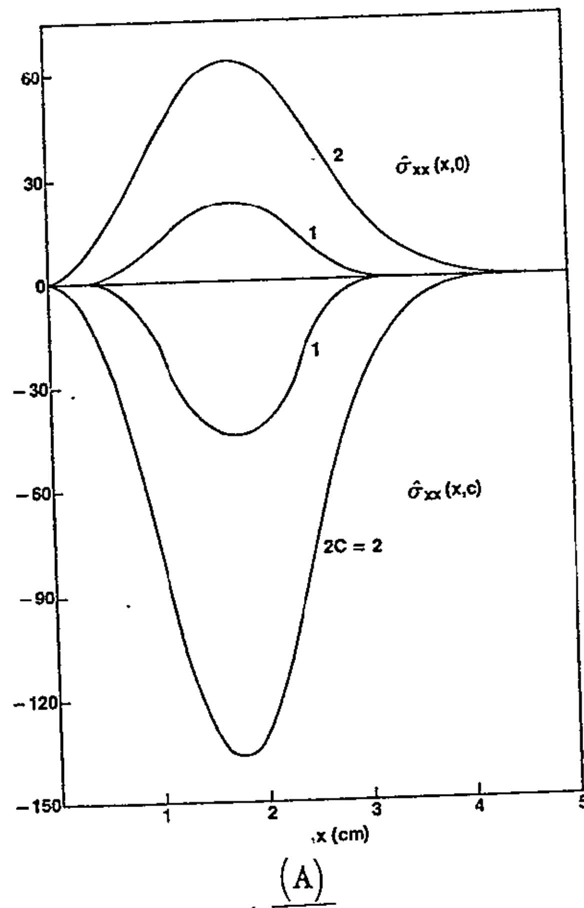

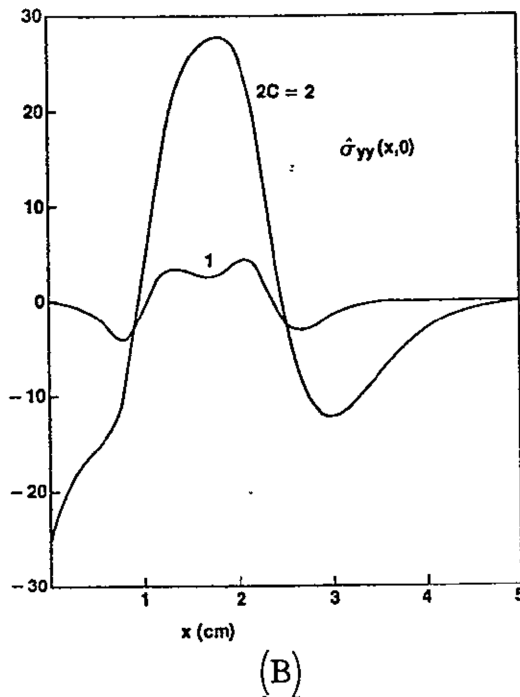

FIGURE 14: Stress* distributions arising from the "ideal" profile of Figure 13. For wide samples, very large stresses result.

---

* The stresses are all normalized to the dimensionless parameter $\hat{\sigma} = \sigma/\alpha E$, where α is the thermal expansion coefficient and E is Young's modulus.

We note, however, that for very narrow samples the stresses are very low for much of the region near the melt. For example, if 2C = 1 cm, stresses would be below the yield point for the entire ribbon since the region where stresses are largest occurs at lower temperatures where the yield stress is high. While growth of 1 cm wide ribbons seems counter to current development efforts, which are towards wider and wider ribbons, it is conceivable that large throughput could still be achieved with 1 cm wide ribbons. One method would be through multiple ribbon growth; for example 40 1 cm wide ribbons grown simultaneously at 2.5 cm/min would lead to 100 cm^2/min growth. Such throughputs have been deemed as "economic" throughputs [12]. While the thought of growing 40 ribbons simultaneously is staggering, the RTR process is quite adaptable to multiple ribbon growth. Multiple growth of ribbons by the RTR process is relatively simple (and even routine) at present, and virtually no additional difficulty is encountered as opposed to ribbon processes requiring a die for shaping. Of course, a much larger number of ribbons must now be processed and handling is increased. Such extreme methods would only be employed, however, if it can be shown that such an ideal profile would actually result in significantly improved crystal quality and photovoltaic efficiency. The application of this technique is limited to roughly the above parameters; 1 cm wide at 2.5 cm/min. Investigation of higher growth rates leads to unreasonably narrow samples while wider samples demand slower growth rates which, assuming a constant throughput of 100 cm^2/min., means the overall processing width is excessive.

1.5.1 Profiles for Wide Ribbon Growth

If wide ribbons are to be grown, the preceding discussion indicates that achieving low stresses near the melt with high growth rates is impossible.

The former requires nearly linear, very low gradient profiles while the latter necessarily requires an initially very steep profile with subsequent large non-linearities. From the studies presented here, the only principle which can be seen to be effective for wide samples is to limit all non-linearities to a region as close as possible to the melt, achieving a linear profile as rapidly as possible. For example Figure 15 indicates several profiles which restrict non-linearities closer to the melt until, for T_3, only a short positive curvature transition remains. T_1 and T_2 represent the range of profiles currently utilized for RTR growth while T_3 represents a more idealized profile. Figures 16a and b indicate stress distributions for each of these profiles for a 6 cm wide ribbon. Profile T_2 produces much reduced stresses compared to those of T_1 while those of T_3 become very small. Consequently, achievement of a thermal profile with a steep initial gradient to achieve high growth velocities but then immediately changing to a gentle linear slope can result in large throughput and very low stresses. Creating such a profile, however, would require a combination of active cooling adjacent to the melt and active heating in the linear region -- a task requiring ingenious furnace and auxiliary heat transfer device design.

1.6 Buckling of RTR Ribbons

The pronounced buckling of RTR ribbons, as illustrated in Figure 1, is most dramatic for wide ribbons grown at high velocity. It is also sensitive to the profile shape. For example, on 2.5 cm wide ribbons we can go from a condition of buckling to nearly flat growth simply by

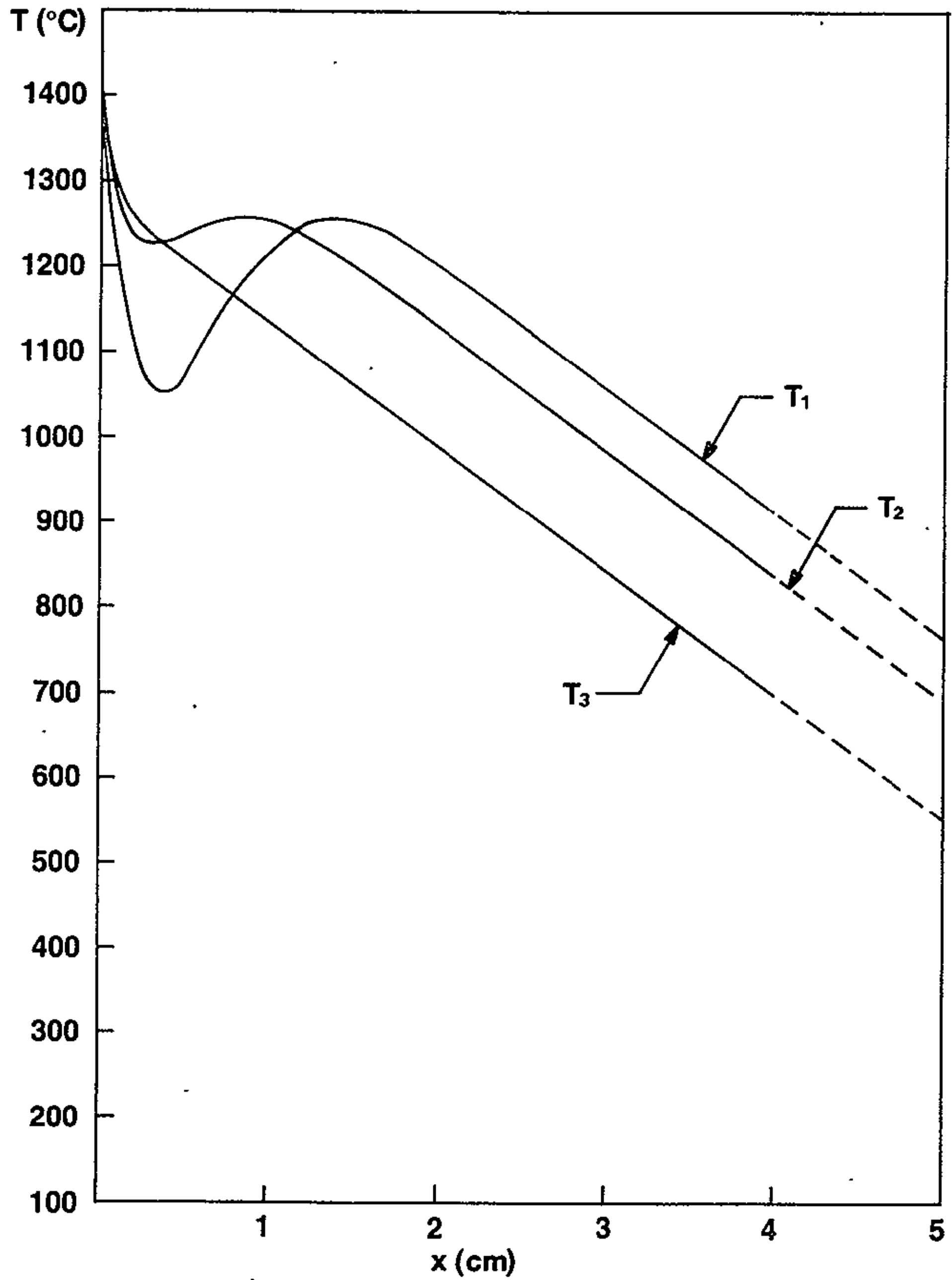

FIGURE 15: Profile improvements which can lead to improved, wide ribbon growth conditions. T2 represents conditions expected when the melt is moved closer to the postheater. T3 represents an ideal profile which achieves high growth velocity and low stresses (see Figure 16).

ORIGINAL PAGE IS
OF POOR QUALITY

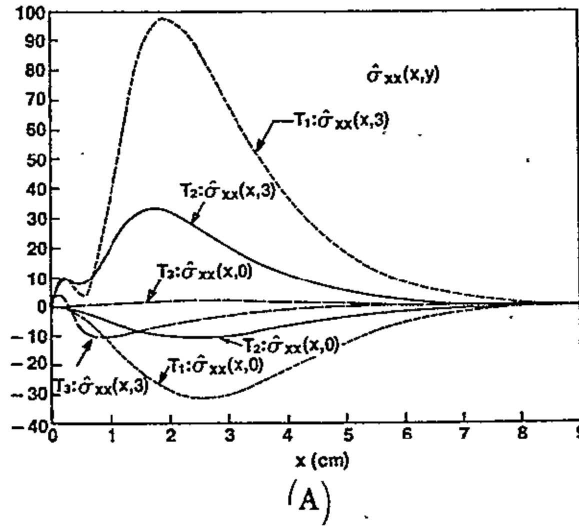

(A)

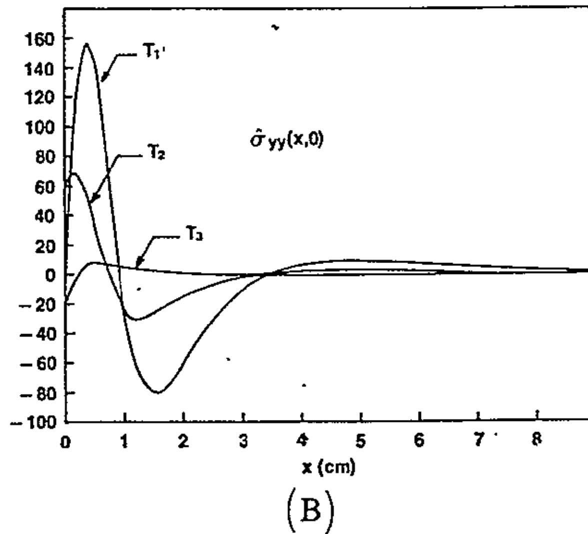

(B)

FIGURE 16: Stress* distributions for the profiles of Figure 15.

* The stresses are all normalized to the dimensionless parameter $\hat{\sigma} = \sigma/\alpha E$, where α is the thermal expansion coefficient and E is Young's modulus.

moving the melt closer to the postheater. This is analogous to a change in thermal profile from that of T_1 to T_2 of Figure 15. Buckling has also been observed to cease once the dendritic growth regime [13] has been achieved. This occurs at the highest possible growth rate for a given thermal profile and is coincident with substantial alterations in thermal profile and melt configuration. These alterations are due to significant latent and sensible heat transport. The absence of buckling in this mode may be considered to result from one or both of two mechanisms. First,the alteration of thermal profile which occurs is such that stresses should be reduced. Second, the occurrence of dendritic formation leads to a "ribbed" structure which will tend to stiffen the ribbon against buckling [14].

1.6.1 Buckling Mechanisms

The buckling of ribbon under the action of in situ thermally induced stresses is readily understood. Figure 17 shows a flat element of ribbon under a uniform compressive stresses σ and $\lambda\sigma$. If the compressive stresses are small, then the plate can absorb the energy of compression as elastic strain energy and any tendency to buckle will be opposed because the energy of bending (due to the internal stress) is larger than the virtual work that would be expended in bending the ribbon. Consequently, system energy would have to increase indicating system stability. On the other hand, at a critical level of compressive stress, the situation is reversed; under bending the total energy of the system can decrease and buckling may occur.

The treatment of elastic instabilities is highly devleoped, but only simple situations are conducive to exact analytic treatment.

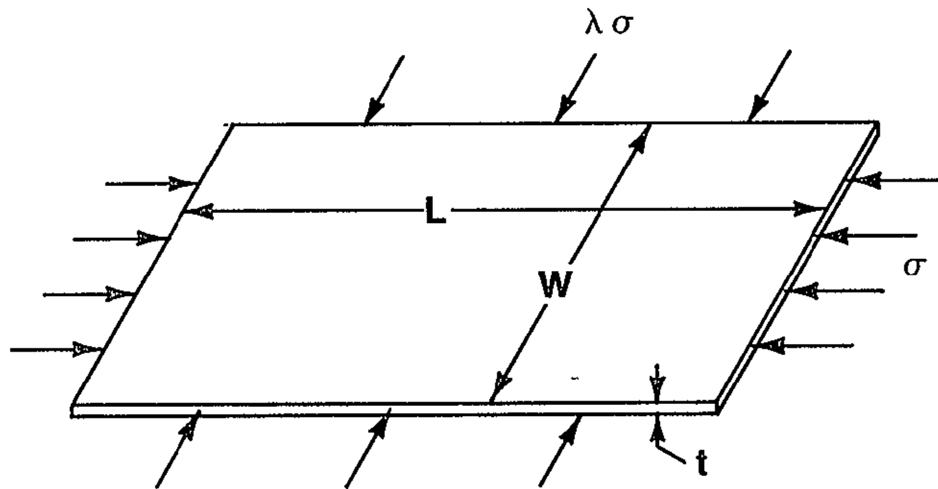

FIGURE 17: Thin plate acted on by uniform compressive stresses in the plane of the plate. For stresses exceeding a critical stress, σ_{cr}, the plate becomes unstable and buckling can occur.

For example, analysis of a thin rectangular plate (Figure 17) of thickness t, with a compressive stress σ acting along its length ℓ, and a stress $\lambda\sigma$ acting along its width W, leads [15] to a critical compressive stress which can be written (for $\frac{1}{2}<\lambda<2$)

$$\sigma_{cr} = k \frac{E\,\pi^2 t^2}{3(1-\nu^2)W^2} \equiv k\sigma_o \qquad (14)$$

where

$$k \equiv \frac{\frac{1}{4}\left(1 + \left(\frac{W}{\ell}\right)^2\right)^2}{\left(\frac{W}{\ell}\right)^2 + \lambda}$$

and ν is Poisson's ratio (assumed to be .25). (In this section, compressive stresses are usually of interest and are designated as positive, contrary to previous usage). The characteristic stress σ_o, may be evaluated if we assume typical conditions. Let us assume $E = 1.17\times10^{12}$ dynes/cm^2, t = .015 cm, and ν = .25 then

$$\sigma_o = \frac{9.24\times10^8}{W^2} \text{ dynes/cm}^2$$

$$\delta_o = \frac{197}{W^2}$$

and

$$\sigma_{cr} = 9.24\times10^8 \frac{k}{W^2} \frac{\text{dynes}}{\text{cm}^2} \qquad (15)$$

or

$$\delta_{cr} = 197 \frac{k}{W^2}$$

The restriction of the above relation to $\frac{1}{2}<\lambda<2$ is due to the nature of the complete instability analysis, which allows for numerous solutions, and a criterion of lowest energy must be determined. For the range given, a simple solution

is possible and assumes simple $\frac{1}{2}$-wave distortion across the width and length. If $\lambda<\frac{1}{2}$, it is shown that

$$\sigma_{cr} > (1-\lambda)\ \sigma_o \tag{16}$$

Consequently, if $\lambda<0$ (i.e. a tensile stress is applied across the width) the tendency towards buckling is substantially inhibited.

Application of these results to ribbon growth can only be in a semi-quantitative manner. Consider, for example, the results of Figures 12a and 12b for 2, 4, and 6 cm wide ribbons. From these figures we note that compressive stresses arise primarily in the center of the ribbon and away from the melt zone. Large compressive stresses do occur for the 2 and 4 cm wide samples along the edges near the melt, while lateral stresses are all tensile in this region. Estimating the parameters to be utilized in evaluating equations (14) and (15) is acomplished by taking an "average" stress of 50% of peak and estimating the corresponding "width" and "length" parameters with help from the "typical" curves of Figure 4. For example, for the 2 cm wide sample with compressive stresses on the outer edge, we estimate an average longitudinal stress of δ = 40, a length ℓ = .5 cm and a width W = .2 cm (from Figure 4). While the lateral stresses appear high in Figure12b, at the edge region these stresses are considerably reduced and we take $\lambda \simeq -.1$. Consequently we use equations (15) and (16) to estimate that

$$\delta_{cr} \simeq \frac{1.1\ \delta_o}{(.2)^2} = 5417$$

Since $\delta_{cr} >> \delta$ for this region, buckling is not likely to occur here. Applying the same estimating procedures to the same 2 cm wide sample

for the compressive region of the central portion of the ribbon we see that lateral stresses and longitudinal stresses are both compressive and act over larger regions. Here we estimate $\delta \approx 11$, $\lambda \approx 1.5$, $\ell \approx W = 1$ cm. In this case we utilize equation (14) finding $k \approx .4$ and $\delta_{cr} \approx 79$. Again we see that the critical stresses appear to be much larger than are expected in a 2 cm wide sample and buckling should not occur.

As the sample width becomes larger, buckling becomes more likely. Going to the 6 cm wide sample of Figure 12 we see that compressive stresses occur only in the central portion of the ribbon and that both σ_{xx} and σ_{yy} are compressive. For this sample we estimate $\delta \approx 15$, $\lambda \approx 2$, $\ell \approx 3$ cm, $W \approx 3$ cm. This gives $k \approx .5$ and $\sigma_{cr} \approx 11$. Consequently, under these conditions, buckling would be expected.

1.6.2 Discussion

While the simple buckling instability considerations presented here indicate critical stresses of roughly the same magnitude as predicted by the elastic analyses, application of these equations generally indicates that buckling is rather unlikely except for samples of considerable width. On the contrary, experiment indicates that ribbon buckling can occur even in 2 cm wide ribbons on occasion. Consequently, the threshold for buckling is of the correct order-of-magnitude, but fails to account for all observations. This discrepancy might be accounted for on the basis of a more exact buckling analysis which can more accurately account for the large peak stresses which occur.

1.7 Conclusion

Elastic stress distributions described for a variety of ribbon thermal profiles indicate that ribbon stresses do not increase with sample width as rapidly as previously supposed. The calculated stress levels are also shown to be usually below yield stresses computed on a strain rate basis, thus indicating that stresses are not rapidly relieved by plastic deformation. Two "ideal" profiles were described, one a profile which could theoretically result in <u>no</u> plastic flow but limited to narrow ribbon growth, and a second which is applicable to wide ribbon growth. Each profile requires deployment of ingenious techniques for its achievement. Finally, the classical theory of elastic instability has been applied to the resulting stress distributions in a semi-quantitative manner with partial success. Correct order-of-magnitude threshold stresses are obtained, but buckling of narrow ribbons cannot be accounted for.

2.0 CRYSTAL GROWTH

A crystal growth rate of ~ 55 cm^2/min has been reached in two growth runs. The widths of the grown crystals were 7.3 cm, the growth rate 7.6 cm/min. Due to the limited length of our samples, this growth rate was achieved for only ~ 3 - 4 cm. However, steady state growth was achieved, and the molten zone was stable. The sample was lightly dendritic, but the dendrites were not uniformly distributed over the width of the ribbon. Over one-half of the sample width, the dendrites grew in an ordered array, parallel to the growth direction, roughly 1 mm apart. Over the other half, however, the dendritic growth was disordered. Ordered dendritic growth can probably be established at somewhat higher growth rates, (and by improving the uniformity of the temperature profile across the ribbon). since the dendrites started growing only about 6.8 cm/min.

The grain size of RTR silicon ribbon grown from CVD material, was found to depend on the quality of the feedstock. The best ribbon was grown from feedstock that did not contain CVD growth spikes or nodules. The nodules are visible as black dots on the photograph of a CVD ribbon shown as Figure 18. Figures 19 a, b are Wright-etched samples of ribbons grown from feedstock containing growth spikes (19a) and feedstock which did not contain growth spikes (19b). The growth spikes/nodules were essentially eliminated by increasing the deposition rate of the CVD ribbon, which produced a finer-grained ribbon.

2.1 CONTROLLED DENDRITIC GROWTH

By controlling the temperature gradient in the molten zone and through the solid-liquid interface, RTR silicon can be grown in a dendritic regime. The dendrites grow ahead of the normal solid-liquid interface and therefore can determine the microstructure of the growing ribbon. The number and size of the dendrites, as well as their distribution, are controlled by the temperature profile across the width of the ribbon

ORIGINAL PAGE IS
OF POOR QUALITY

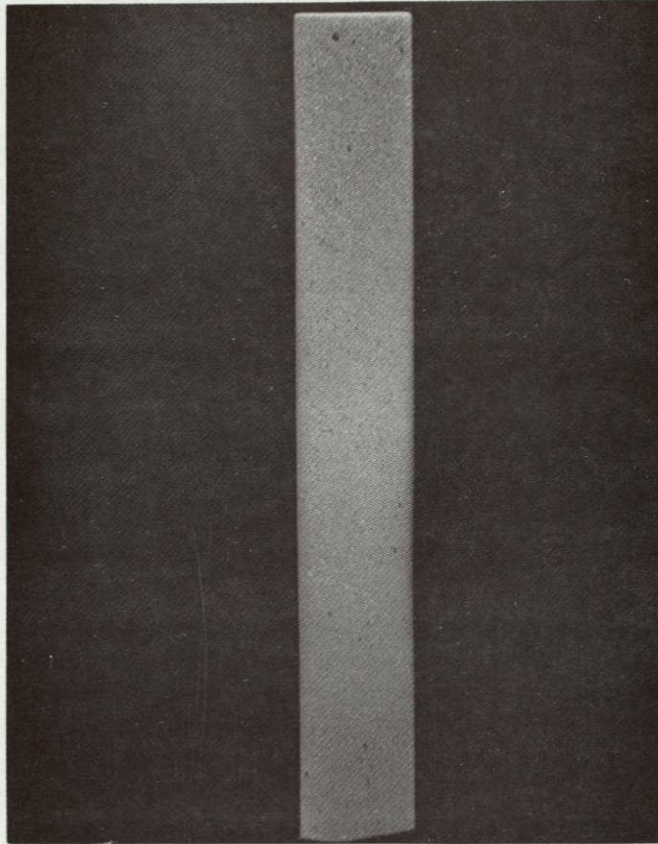

FIGURE 18: CVD RIBBON: THE BLACK DOTS ARE THE NODULES CONTAINING THE GROWTH SPIKES REFERRED TO IN THE TEXT.

ORIGINAL PAGE IS
OF POOR QUALITY

FIGURE 19a: RTR SAMPLE GROWN FROM FEEDSTOCK CONTAINING GROWTH SPIKES.

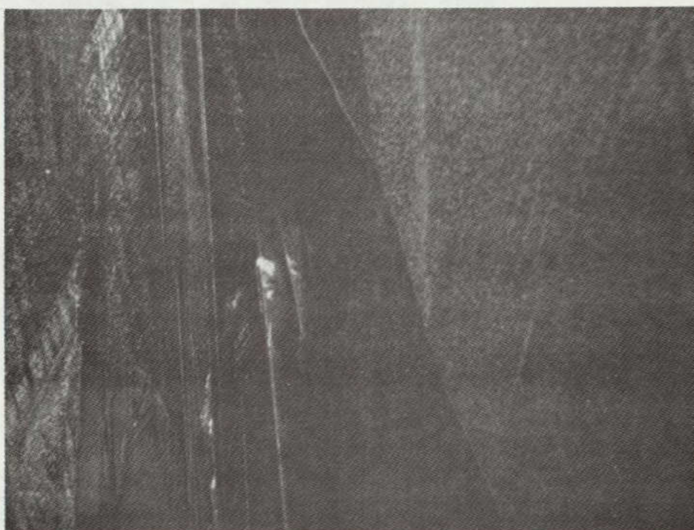

FIGURE 19b: RTR SAMPLE GROWN FROM FEEDSTOCK WHICH DID NOT CONTAIN GROWTH SPIKES.

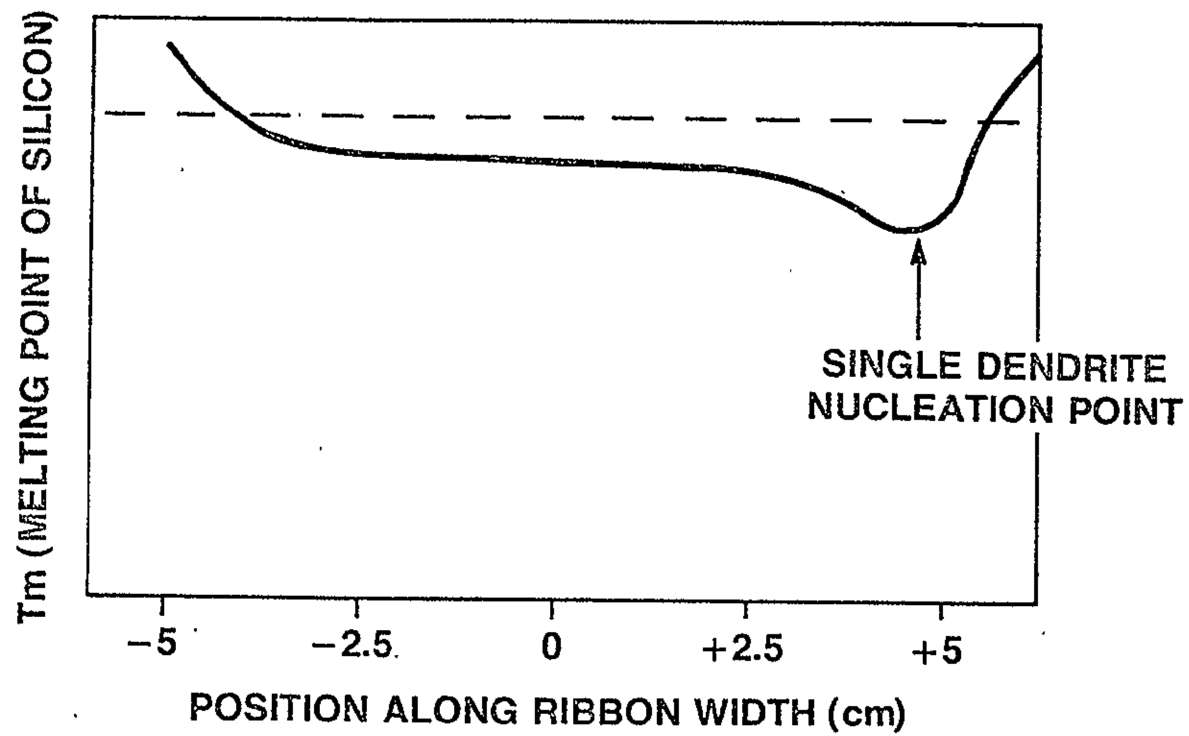

FIGURE 20: Temperature profile across ribbon width.

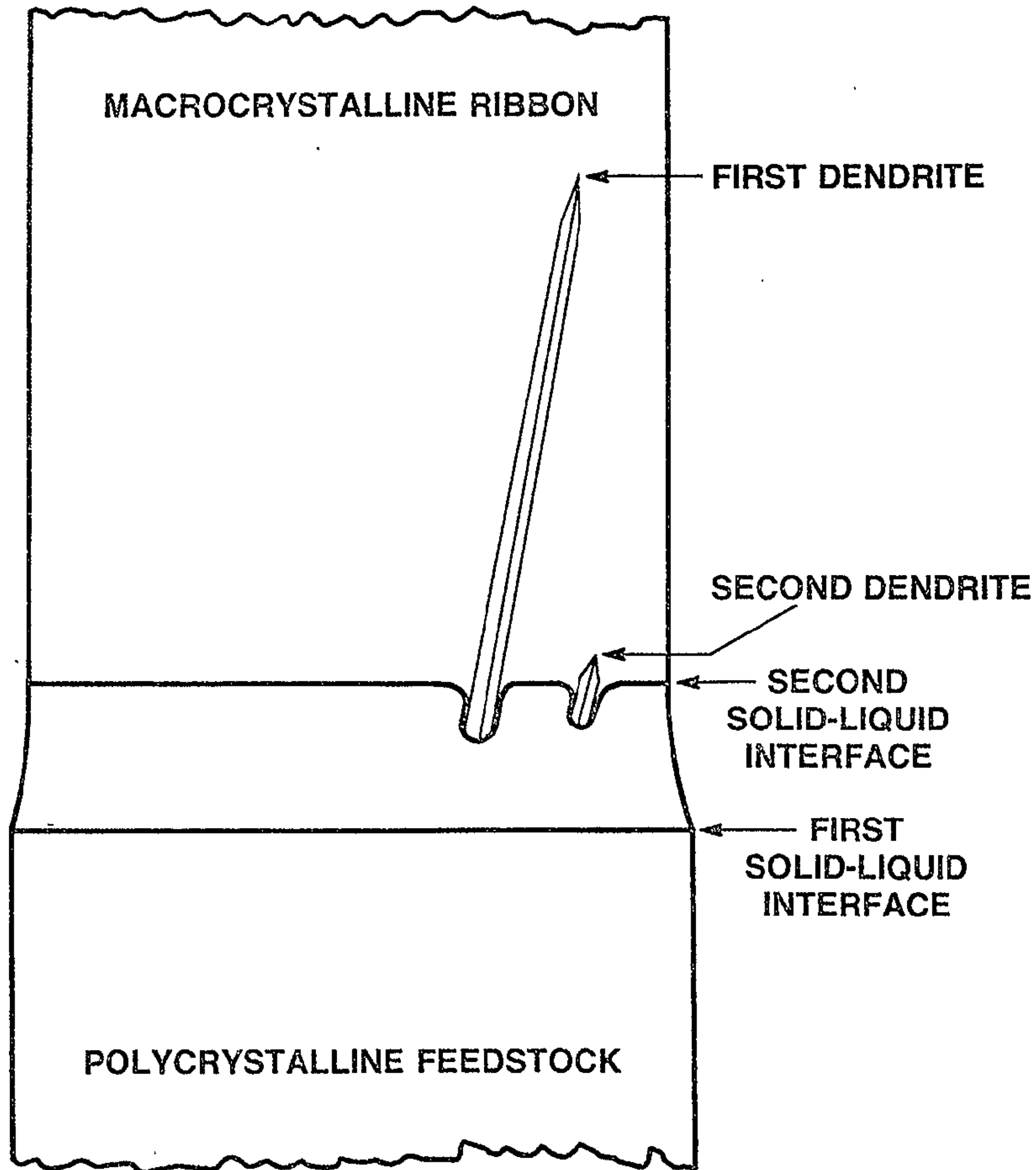

FIGURE 21: DENDRITE NUCLEATION

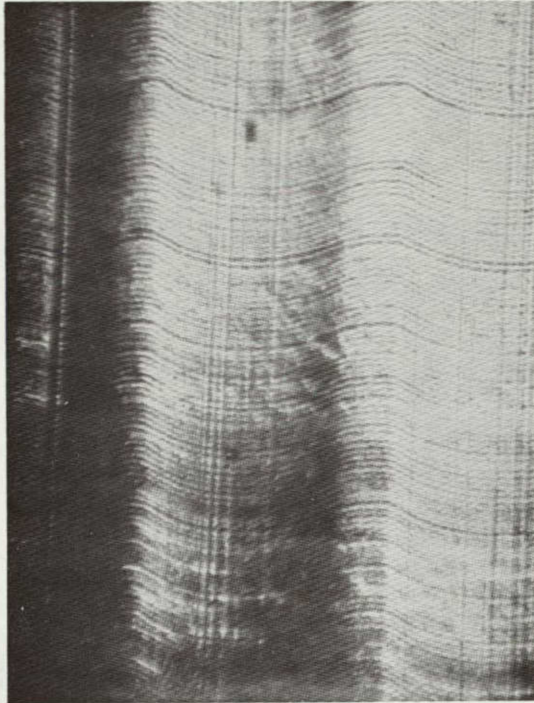

FIGURE 22: Surface Topography - Controlled Dendrite Growth

ORIGINAL PAGE IS
OF POOR QUALITY

½mm

E8782

FIGURE 23: Surface Topography - Random Dendrite Growth

significantly to the generation current. By contrast, planar defects under the dendrites are relatively benign. Figure 26 is an end view of such a defect, taken at 50° incidence. The etching depth was only ~ 6 μm, indicating a relatively low energy defect. These qualitative conclusions are in agreement with measurements of the electrical activity of these defects taken with an SEM in the EBIC mode [16]: grain boundaries are strongly active, while twin planes/stacking faults are not detected.

These SEM micrographs show that, with controlled dendritic growth, the more harmful defects (grain boundaries, high density dislocations) are concentrated in a narrow area between dendrites, covering roughly 10% of the total available area. Previous measurements have shown that in the worst case, such areas still generate 50% of the potential photocurrent [17]. Thus the overall generation current loss due to high defect areas between the dendrites is on the order of 5%.

ORIGINAL PAGE IS
OF POOR QUALITY

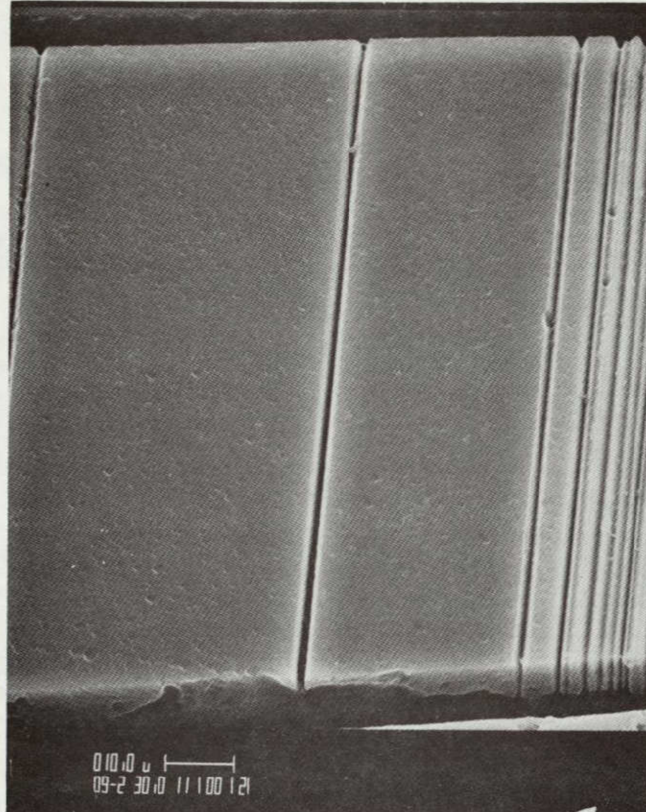

FIGURE 24: Dendrite Microstructure

ORIGINAL PAGE IS
OF POOR QUALITY

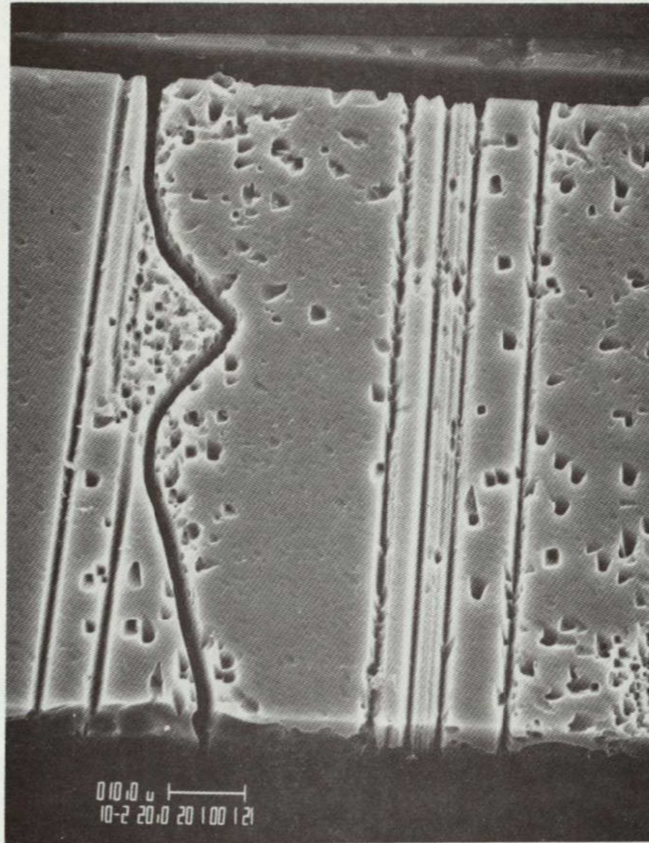

E8784

FIGURE 25: Grain Boundary

ORIGINAL PAGE IS
OF POOR QUALITY

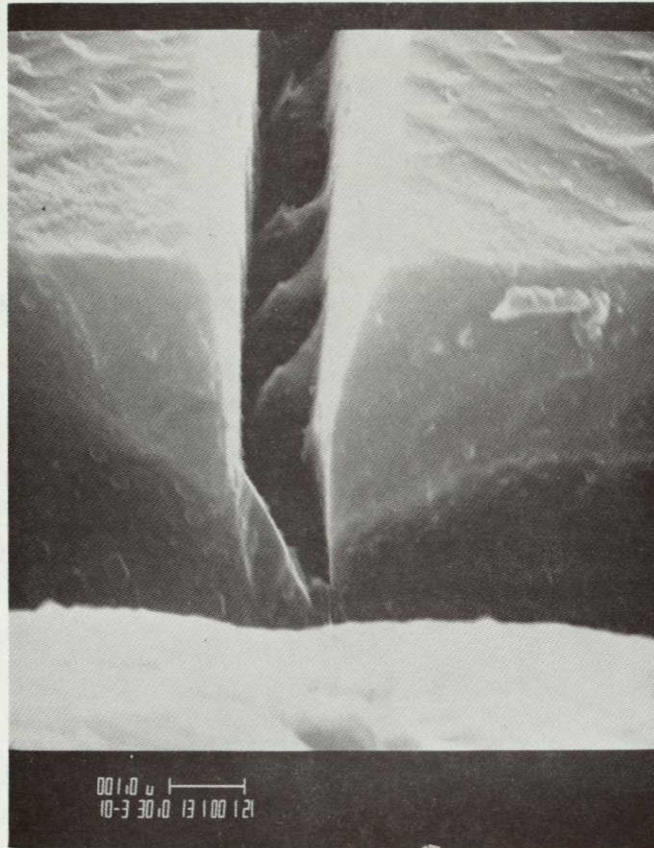

E8785

FIGURE 26: End View of Planar Defect

7) Sintering of the silicon tape in a reducing atmosphere to increase the strength and density of the tape and to reduce the oxygen content.

8) Densification of the tape via vapor phase growth onto the ribbon.

Steps 2 - 6, which involve the formation of the tape, are very simple and low cost. The key questions are purity of the resulting silicon tape, and the necessity of step #8, densification.

The purity of the resulting silicon will, for the most part, be dictated by the choice of a binder and the burn-off procedure. It seems very probable that a binder can be developed which can be totally volatilized and oxidized. Use of distillation processes to obtain a very high purity binder initially, should reduce residual impurities to acceptable levels.

Step #8, densification, may or may not be necessary. Previous experimentation has indicated that it would be required.

Some investigations have been initiated which will attempt to determine the basic feasibility of this process. The feasibility of producing sintered silicon tape has already been verified since it has been found that Airesearch Casting Company (a division of Garrett) has previously produced such tape. Their application, however, is for production of silicon nitride tape and purity is not a major concern. To test the feasibility of this tape for our process, we will supply Airesearch with high purity silicon powder to be fabricated into silicon tape. Precautions will be taken to choose a high purity binder and a burn off -- sintering cycle which should provide silicon tape of high purity. We will subsequently attempt to regrow these tapes with or without the densification procedure. If growth is successful, electrical evaluations will then be made.

4.0 IMPURITY CONTROL IN RTR SILICON

The RTR process is similar to float zone crystal growth in that the molten silicon is not in contact with a container or die which might contaminate it. Thus the main source of impurities is the polyribbon feedstock itself. At present, the polycrystalline feedstock is grown by chemical vapor deposition on a molybdenum substrate. Neutron Activation Analysis (N.A.A.) on CVD feedstock has shown Mo contamination in the range of 5 - 20 ppmw (~ $10^{16}/cm^3$). R. H. Hopkins and co-workers have shown that Mo impurities at a concentration as low as $10^{12}/cm^3$ reduce the cell efficiency by 15% [18]. Thus, for high efficiency solar cells, the Mo level may have to be reduced by several orders of magnitude.

Mo may be incorporated into the Si ribbon by several mechanisms: Mo vaporization, caused by plasma arcing due to high RF fields in the reaction chamber; autodoping due to chlorine transport of Mo; or solid-state diffusion from the Mo substrate directly into the silicon ribbon, possibly along the grain-boundaries of the polycrystalline silicon.

The first two mechanisms would result in Mo distributed randomly (in the case of Mo vaporization), or uniformly in the bulk of the silicon ribbon (in the case of autodoping). Secondary Ion Mass Spectroscopy, however, has shown a strong dependence of the Mo concentration on distance from the Mo-Si interface (See Figure 27). This positional dependence implies that direct solid-state diffusion across the Mo-Si interface may be a primary mechanism for Mo doping of the silicon ribbon.

In an initial experiment, 1 - 2 mils were removed from the silicon ribbon surface by different techniques: HCl vapor etch, mechanically

polishing the ribbon surface, wet chemical (HNO_3, HF, Acetic Acid) etch, and plasma etching in a CF_4-O_2 glow discharge [19]. Neutron Activation Analysis showed that both the chemical etch and the plasma etch reduced the Mo impurity level to below the N.A.A. detection limit (~ 1 ppmw Mo in this case).

Ahother approach for reducing the Mo contamination is to deposit a diffusion barrier onto the Mo belt prior to silicon deposition. Silicon nitride was chosen as the diffusion barrier since it is easy to deposit, does not introduce a new element into the system and is an excellent diffusion barrier [20], An 800 - 850Å layer of silicon nitride was deposited at 750°C using low pressure chemical vapor deposition. A silicon ribbon was then deposited on the Si_3N_4-Mo belt using standard deposition conditions. The polyribbon separated intact from the Si_3N_4-Mo substrate. The polyribbon was then routinely re-grown, using the RTR apparatus at 1"/min. The first photovoltaic cell was recently fabricated on this material, (See Section 6.0). It had an efficiency of 6%, with I_{SC} ~ 16.4 mA/cm^2. V_{OC} ~ 0.54 volts. These results are significantly improved over ribbons grown from unprotected feedstock, which typically have η ~ 4%. However, the efficiency is still low, indicating that further progress needs to be made.

The Si_3N_4 coating has the additional benefit of protecting the Mo substrate from exposure to Si or SiH_xCl_y vapor. This should greatly extend the useful life of the Mo substrate.

The use of a Si_3N_4 coating on Mo substrates may introduce new problems. One possible problem area may be microcracks in the Si_3N_4 film. Figure 28 is a photograph of such a crack in the Si_3N_4 film after deposition and separation. The microcracks were few and far apart; their width is

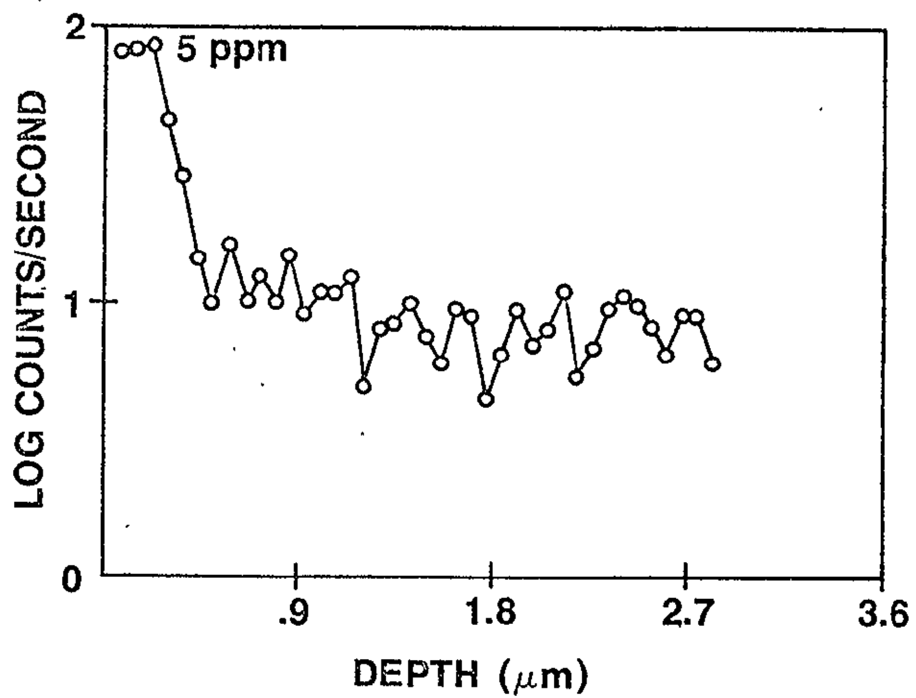

FIGURE 27: Mo Concentration - Depth Profile

ORIGINAL PAGE IS
OF POOR QUALITY

ORIGINAL PAGE IS
OF POOR QUALITY

FIGURE 28: Microcrack in Si_3N_4 Film
(440X magnification)

5.0 THE MEASUREMENT OF SHORT DIFFUSION LENGTHS

The OCPV or SPV methods for measuring diffusion lengths cannot be used to measure diffusion lengths below ~ 5 μm [21]. We have applied another method, first used by Logan and Chynoweth on GaP homojunctions [22], to the measurement of diffusion lengths in silicon ribbon. This technique, referred to here as the Depletion Width Modulation (DWM) method, relies on the measurement of the difference between the photocurrent generated by long wavelength, monochromatic light, and the dark current under reverse bias.

Data for sample 784-1 (for AM1 conditions, J_{sc} = 13.0 ma/cm^2, V_{oc} = 0.49 and a fill factor of 75% are shown in Figure 29. The data is an excellent fit to a straight line, confirming the validity of our assumptions. The diffusion length in this case is 2.68 μm. The diffusion length and J_{sc} are listed in Table 1 for three solar cells fabricated on re-grown CVD silicon. Table 1 also contains the carrier concentration of the RTR samples. These data were obtained by plotting $C(V)^{-2}$ vs. V. Since [23]

$$\frac{d\left(\frac{A^2}{C^2}\right)}{d\ V} = 2\ (N_A q\varepsilon)^{-1}$$

N_A can be calculated from the slope of C^{-2} vs. V.

The variation in the measured carrier concentration is small, both from sample-to-sample and along the length of a single ribbon. Moreover, the measured doping level is very close to our target during the CVD process:

$$N_A\ \text{(meas.)} \approx 2 \times 10^{16}/\text{cc},\ N_A\ \text{(goal)}:\ 1.5 \times 10^{16}/\text{cc}$$

These tolerances compare well with the variation which occurs with Czochralski silicon.

The photocurrent of an n+-p cell consists of three components:

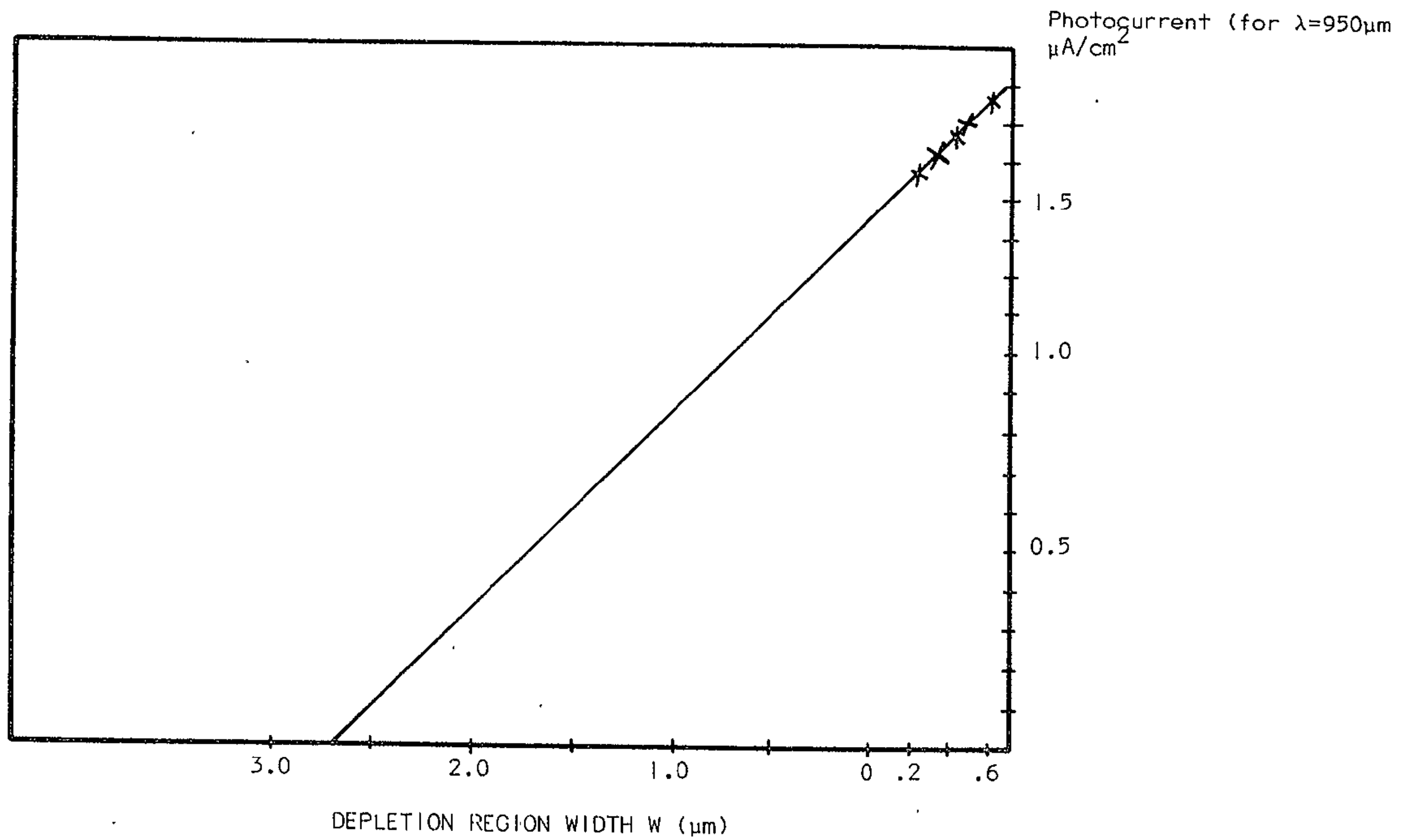

FIGURE 29: DIFFUSION LENGTH MEASUREMENT BY DWM - SAMPLE 784-1

1) Hole current collected from the generation of electron-hole pairs in the n+ region.

2) Current collected from electron-hole pairs generated within the depletion region.

3) Electron current collected from electron-hole pairs generated within the bulk of the p-type substrate.

For the case of uniform generation of carriers - i.e. for long wave-length light - the first contribution is negligible because the diffusion length in the thin, heavily doped n+ region is very short. So, neglecting the term due to hole generation, the photocurrent can be given by:

$$J_{photo} \propto W + L_e$$

where L_e is the electron diffusion length in the p-region

W is the depeltion region width (the substrate thickness is much greater than its diffusion length).

The width of the depletion region is given by:

$$W(V) = \left(\frac{2\varepsilon\ (V_b+V)}{qN_A}\right)^{\frac{1}{2}}$$

where V is taken as positive for reverse bias. The photocurrent will then increase with reverse bias. A plot of J_{photo} vs. W will have an intercept, for $J_{photo} = 0$, at $W = -L_e$.

The experimental procedure is then to first obtain W(V) by measuring the capacitance - voltage characteristics:

$$W(V) = \frac{\varepsilon A}{C(V)}$$

Then, by plotting the photocurrent as a function of W(V) the diffusion length can be determined.

TABLE I: PHOTOVOLTAIC DEVICE DATA

SAMPLE	L_e (measured by DWM)	J_{sc} AM1 ILLUMINATION	N_A
784-1	2.68	13.0	2.13×10^{16}
784-2	3.30	13.8	2.14×10^{16}
780-1	-	13.5	2.16×10^{16}
780-2	3.10	13.1	2.40×10^{16}
780-3	-	13.5	2.21×10^{16}
775-1	-	12.2	2.46×10^{16}

6.0 SOLAR CELLS - FEEDSTOCK GROWN ON BARE Mo SUBSTRATE

The first lot of solar cells made from CVD feedtock (grown on bare Mo substrate) has been fabricated, and efficiencies measured. The results are summarized in Table II. The maximum nominal efficiency of 5% is disappointing, of course, but three important points should be made:

1) Of the three fundamental solar cell parameters affecting efficiency, V_{OC}, J_{SC} and fill factor, the better cells of this lot were well above average in fill factor (74 vs 61%), above average in V_{OC} (.490 vs. .478) but deficient in J_{SC} (13. vs. 26.), all compared to the better cells made on regrown single crystal feedstock. The fill factor, which in conjunction with the open circuit voltage, is a measure of the leakage current present in the solar cell junction provides a very encouraging picture. A semilogarithmic plot of the dark current-voltage characteristics for an RTR solar cell from regrown single crystal feedstock (η = 9%, V_{OC} = .49, J_{SC} = 29.1, FF = 65%) is compared with a cell made from regrown CVD feedstock (η = 4.9%, V_{OC} = .494, J_{SC} = 13.1, FF = 76%) in Figure 30. As can readily be seen, leakage current in the CVD cell is much lower.

2). The short curcuit current is so much smaller than expected that the only reasonable cause could be very short minority carrier diffusion length. A short circuit current of less than 15 mA/cm^2 puts an upper limit on the diffusion length of 20 µm. Since diffusion lengths (and short circuit currents) are commonly seen to be much larger on solar cells made from regrown single crystal feedstock, the cause is <u>almost</u> certainly some kind of chemical contamination in the CVD feedstock. This is consistent with neutron activation analyses which have shown Mo impurity levels in the range of 5 - 20 ppmw.

3) This lot of cells was made by a planar process which was thought to be superior to the mesa process used in the past. This may not be the case. The control cells, consisting of 4 - 6 inch long slabs of single crystal (100) Czochralski silicon, which were processed along with the CVD ribbons, were

TABLE II

SOLAR CELLS FABRICATED ON RTR SILICON GROWN FROM CVD FEEDSTOCK

Planar process, using Si_3N_4 masking, Pd/Ni metallization.

Cell Area: 4 cm^2

CELL I.D.	V_{OC} (volts)	I_{SC} (mA/cm^2)	FF	η (AM1)
789-2	0.494	13.1	0.76	4.9
789-1	0.490	13.0	0.75	4.8
791-1	0.490	13.8	0.70	4.7
718-F-1	0.505	14.2	0.61	4.35
776-3	0.493	12.8	0.68	4.3
780-2	0.487	13.8	0.63	4.2
780-3	0.486	13.5	0.63	4.1
782-4	0.486	12.8	0.64	4.0
773-2	0.485	13.3	0.60	3.9
775-1	0.489	12.2	0.64	3.8
780-1	0.490	13.5	0.54	3.6
776-2	0.496	12.1	0.57	3.4
777-3	0.473	12.9	0.52	3.2
784-1	0.488	11.4	0.57	3.2
775-2	0.477	12.8	0.49	3.0
Control Czochralski	0.515	26.0	0.74	10

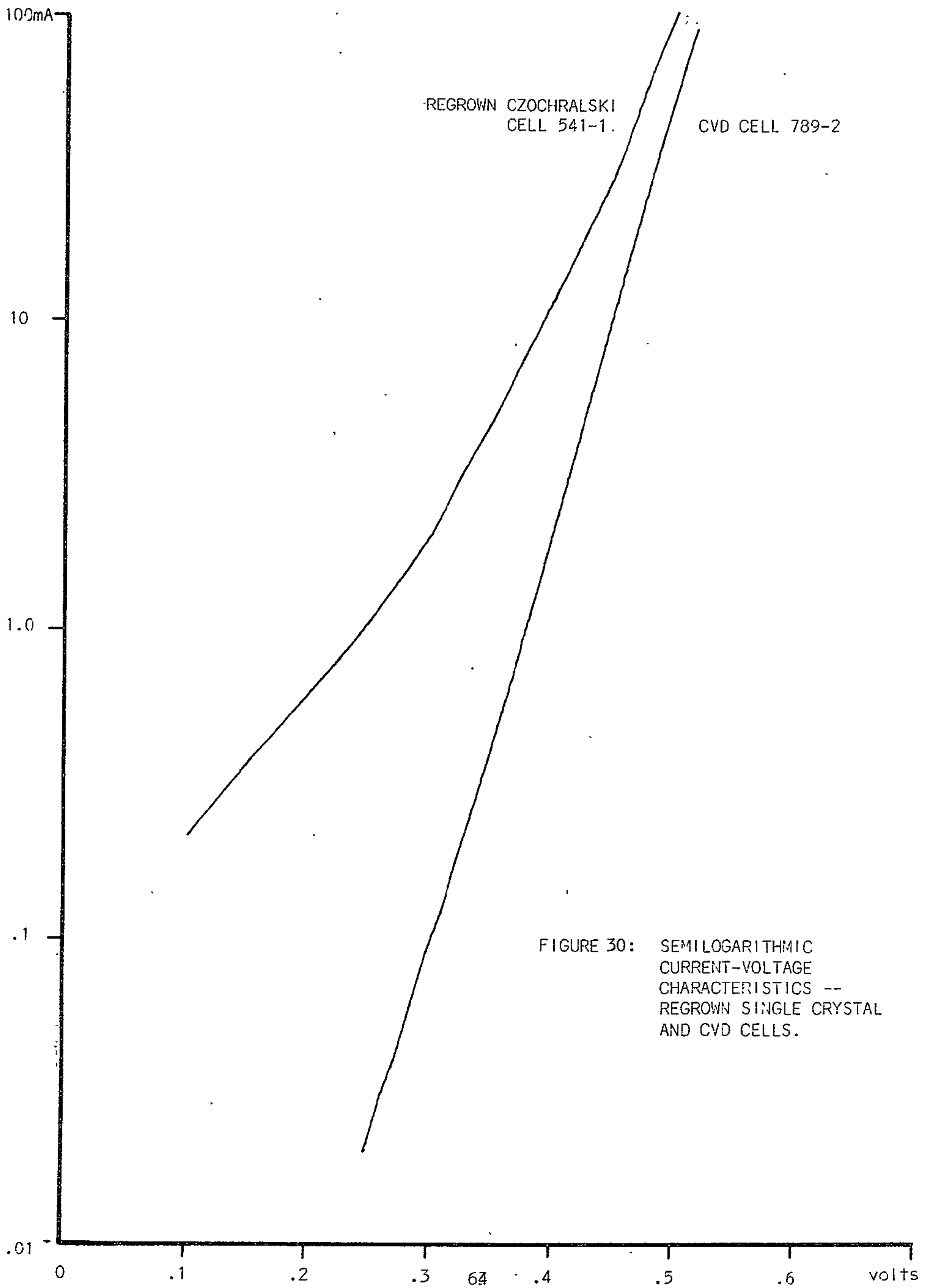

FIGURE 30: SEMILOGARITHMIC CURRENT-VOLTAGE CHARACTERISTICS -- REGROWN SINGLE CRYSTAL AND CVD CELLS.

ORIGINAL PAGE IS
OF POOR QUALITY

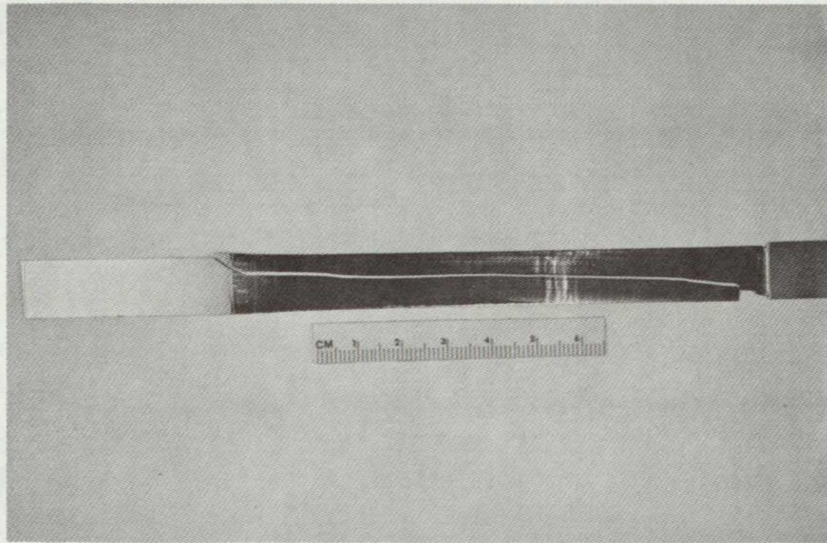

FIGURE 31a: RIBBON FRACTURE -- PARALLEL TO GROWTH

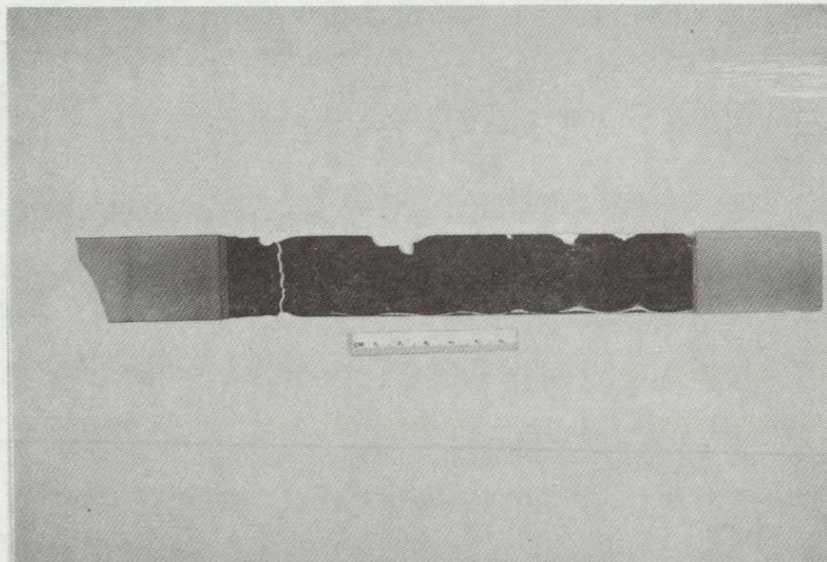

FIGURE 31b: RIBBON FRACTURE -- NORMAL TO GROWTH

requiring a drying step. Also, for steps in the processing which do require a drying step (following an ultra pure deionized water rinse), an alternate drying procedure will be used. Instead of a forced nitrogen blow-dry step which is a one-ribbon-at-a-time process that stresses the ribbon and causes fractures, a much more gentle, multiple ribbon drying step using a freon vapor degreaser system will be used. This should reduce breakage substantially, and increase the number of ribbons that can be processed (or increase the speed of processing ribbons).

There is a second source of ribbon breakage which has received attention, and that is due to the excess weight of the un-regrown tabs of CVD feedstock which accompany every CVD ribbon. These are 1 - 2 inches of dead weight microcrystalline silicon which weighs down the ribbon particularly when picked up in the center, and exerts stress resulting in fracture. We intend to scribe tabs off using a YAG laser scriber apparatus. The YAG will also be used for cutting regrown ribbons to uniform lengths, particularly for the ion implanter, which will not take samples longer than 7 inches. YAG scribing has been used successfully on CVD feedstock, macrocrystalline regrown ribbons, and, of course, single crystal silicon.

6.1 SOLAR CELLS - FEEDSTOCK GROWN ON Si_3N_4 - COATED SUBSTRATE

In Section 4.0, we described the use of Si_3N_4 as a diffusion barrier to prevent contamination of the silicon ribbon by Mo. One solar cell has been fabricated on RTR silicon re-grown from feedstock deposited on an Si_3N_4 coated Mo substrate. This cell had an efficiency of 6%, with V_{OC} = 0.545, J_{SC} = 16.4 mA/cm^2 and a fill factor of 67%. The short circuit current is still too low, indicating that the diffusion barrier was not 100%

effective in preventing Mo contamination. This was confirmed by Neutron Activation Analysis which indicated 15.6 ppmw of Mo in another sample grown from polyribbon deposited on Si_3N_4 coated substrate. These results indicate incomplete coverage of the Mo substrate. We will continue these experiments, optimizing the uniformity of the Si_3N_4 coating and increasing its thickness.

REFERENCES

1. R. W. Gurtler, A. Baghdadi, R. J. Ellis, and I. A. Lesk, J. Electronic Materials, Vol. 7, No. 5, (1978), 441.

2. A. Baghdadi, R. W. Gurtler, R. N. Legge, R. J. Ellis, and B. L. Sopori, Proceedings Thirteenth IEEE Photovoltaic Specialists Conference, (1978), 363.

3. A. D. Morrison, K. V. Ravi, C. V. Hari Rao, T. Surek, D. F. Bliss, L. C. Garone, and R. N. Hogencamp, Annual Report, ERDA/JPL 954355/76-11 (1976) 11.

4. M. M. Myshlyaev, V. I. Nikitenko, and V. I. Nesterenko, Phys. Stat. Sol., 36, (1969), 89.

5. C. D. Graham, Jr., S. Kulkarni, G. T. Noel, D. P. Pope, B. Pratt and M. Wolf, 2nd Quarterly Report, ERDA/JPL-954506-76/2 (1976).

6. W. D. Sylwestrowicz, Phil. Mag., Ser. 8, Vol. 7, (1962), 1825.

7. J. R. Patel and A. R. Chaudhuri, J. App. Phy. Vol 34, No. 9, (1963), 2788.

8. B. A. Boley and J. H. Weiner, in: Theory of Thermal Stresses (John Wiley and Sons, N.Y., 1960) 261.

9. B. A. Boley and J. H. Weiner, Op. Cit., 323.

10. K. S. Kunz, in: Numerical Analysis (McGraw-Hill, N. Y., 1957), 275.

11. R. W. Gurtler, A. Baghdadi, Technical Quarterly Report No. 2, ERDA/JPL 954376-76/2, 1976, 25.

12. A. Baghdadi, Proceedings: Ninth Project Integration Meeting, LSA Project (5101-67), (1978), 3 - 89.

13. R. W. Gurtler, A. Baghdadi, R. Legge, B. Sopori, and R. J. Ellis, Technical Quarterly Report No. 6, DOE/JPL 954376-78-1, (1977), 14.

14. P. Masser, Private Communication.

15. H. L. Cox, in: The Buckling of Plates and Shells (Pergamon Press, N.Y., 1963), 21.

16. A. Baghdadi et al., Thirteenth IEEE Photovoltaic Specialists Conference, Washington D.C., June 1978.

17. A. Baghdadi, R. W. Gurtler, R. Legge, B. Sopori, R. J. Ellis, Motorola Quarterly Report No. 8, DOE/JPL No. 954376-78/3, June 1978.

18. R. H. Hopkins et. al., Westinghouse Quarterly Report No. 10, DOE/JPL No. 954331-78/2, March 1978.

19. H. F. Winters, J. W. Coburn, E. Kay, J. Appl. Phys., 48, (12), December 1977.

20. J. T. Milek, Silicon Nitride for Microelectronic Applications (IFI/Plenum, N. Y., 1971).

21. 1977 Annual Book of ASTM Standards, STD F391-37T.

22. Logan and Chynoweth, J. Appl. Phys. 33, p. 1649, (1962).

23. S. M. Sze, Physics of Semiconductor Devices, John Wiley and Sons, N. Y., (1969).

7.0 PROBLEMS

No new technical problems have been uncovered in this period. The Mo contamination problem is receiving continued attention. It is felt that this is the major limiting factor determining RTR solar cell efficiency. The open circuit voltage and fill factor of solar cells fabricated on RTR grown CVD feedstock are satisfactory, but the short circuit current is far too low because of the very short diffusion lengths. Both pre-etching the CVD feedstock (before RTR growth) and growing the CVD polyribbon on a Si_3N_4 coated substrate show potential for reducing the Mo impurity to an acceptable level.

8.0 PLANS

8.1 POLYCRYSTALLINE FEEDSTOCK

We plan to carry out some preliminary experiments with silane as the source gas for CVD formation of the polyribbon. These experiments will allow us to study the impurity level in polyribbon grown in a chlorine-free atmosphere. We will also study the effects of reducing deposition temperature on the efficacy of ribbon separation.

We are also re-cycling the Mo substrate (both bare and Si_3N_4 coated) to determine its maximum lifetime.

8.2 RTR GROWTH

We are installing a new furnace to control the temperature profile in both heating and cooling of silicon ribbons. This furnace is completely sealed, and should allow improved impurity control during RTR crystal growth.

We will also carry out high speed growth runs, with both single and multiple ribbon growth.

8.3 SOLAR CELL PROCESSING

Solar cells are now being made on re-grown CVD feedstock which has been pre-etched. This should result in less contamination and a higher short circuit current. Solar cells will also be started on feedstock deposited on Si_3N_4 coated Mo substrates, both with and without pre-etching.

Single crystal ribbons sawn from a float zone ingot have been re-grown and will be used for solar cell fabrication as well. These will serve as controls and should provide an additional estimate of the potential of RTR grown silicon for solar cells. These will be processed together with re-grown CVD and Czochralski ribbons.

To date we have only reported on solar cells made by conventional diffusion processes (both mesa and planar). Ion implantation is now being used for solar cell fabrication in parallel with the diffusion process. This is a much faster means of making cells and requires less handling. It is expected that these two techniques will continue to be used in parallel in the future.

9.0 NEW TECHNOLOGY

The following New Technology items have been developed on this program:

1. Description - Polygon Scanner System

   Innovator - Dr. Richard Gurtler

   Progress Reports - Technical Progress Report No. 14, October 1977

   Pages - 1, 10, 11A and 11

2. Description - Hemispherical Reflector to Improve Effective Absorption Coefficient of Liquid Silicon

   Innovator - Dr. Ricahrd Gurtler

   Progress Reports - Technical Quarterly Report No. 7, Motorola Report 2256/9, January 1, 1978 - March 31, 1978,

   Pages - Appendix Pages 11 - 13.

3. Description - Dendritic Growth on RTR Silicon

   Innovator: Dr. A. Baghdadi, R. J. Ellis, Dr. R. W. Gurtler

   Progress Reports: Technical Quarterly Report No. 6, Motorola Report No. 2256/8, October 10 - December 31, 1977.

   Pages 14 - 23.

4. Description - Controlled Dendritic Growth

   Innovator: Dr. A. Baghdadi and Mr. R. J. Ellis

   Progress Reports: Monthly Report No. 21, August 1978, JPL/DOE No. 954376.

   Page 1.

5. Description - Coated Substrates for Silicon Deposition

   Innovator: Dr. R. Legge

   Progress Reports: Monthly Report No. 20, July 1978, JPL/DOE No. 954376.

   Page 20.

MILESTONE CHART

Contract No. 954376 MOTOROLA PROJECT NO. 2319-2325

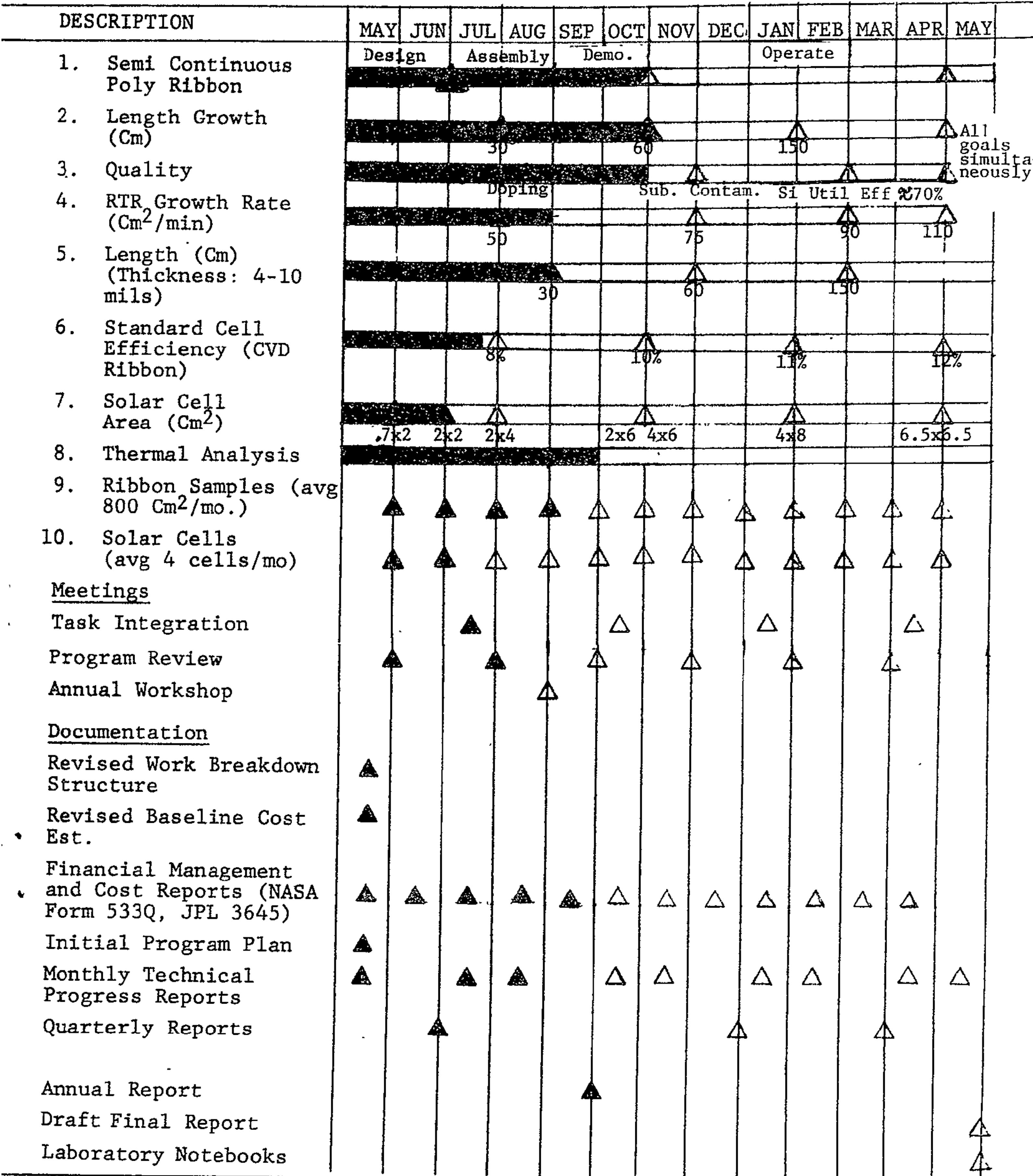

LEGEND SCHEDULE COMPLETED DELIVERY SCHEDULE △ DELIVERED ▲